

Beyond Independent Genes: Learning Module-Inductive Representations for Gene Perturbation Prediction

Jiafa Ruan¹ Ruijie Quan¹ Zongxin Yang^{2†} Liyang Xu¹ Yi Yang¹

¹ReLER, CCAI, Zhejiang University

²DBMI, HMS, Harvard University

Abstract

Predicting transcriptional responses to genetic perturbations is a central problem in functional genomics. In practice, perturbation responses are rarely gene-independent but instead manifest as coordinated, program-level transcriptional changes among functionally related genes. However, most existing methods do not explicitly model such coordination, due to gene-wise modeling paradigms and reliance on static biological priors that cannot capture dynamic program reorganization. To address these limitations, we propose **scBIG**, a module-inductive perturbation prediction framework that explicitly models coordinated gene programs. scBIG induces coherent gene programs from data via Gene-Relation Clustering, captures inter-program interactions through a Gene-Cluster-Aware Encoder, and preserves modular coordination using structure-aware alignment objectives. These structured representations are then modeled using conditional flow matching to enable flexible and generalizable perturbation prediction. Extensive experiments on multiple single-cell perturbation benchmarks show that scBIG consistently outperforms state-of-the-art methods, particularly on unseen and combinatorial perturbation settings, achieving an average improvement of 6.7% over the strongest baselines.

1. Introduction

Predicting transcriptional responses to gene perturbations is a core problem in functional genomics, with broad applications in gene function discovery (Dixit et al., 2016; Replogle et al., 2022), regulatory mechanism analysis (Aibar et al., 2017; Theodoris et al., 2023), and therapeutic development (Lotfollahi et al., 2023; Qi et al., 2024). Recent advances in CRISPR-based perturbation technologies and single-cell RNA sequencing enable high-resolution mea-

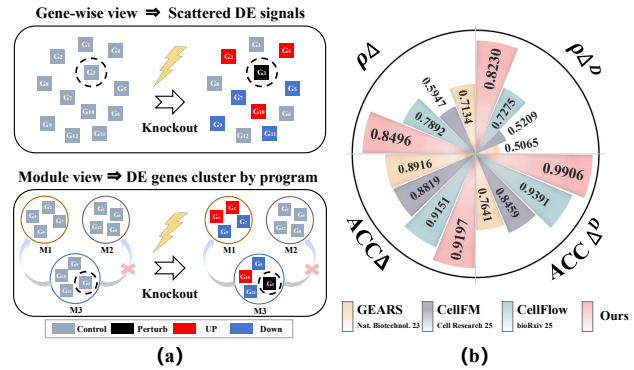


Figure 1. (a): Comparison between gene-wise view and module view in perturbation responses. **Black** indicates the perturbed gene, **red** indicates upregulation, and **blue** indicates downregulation. (b): Quantitative comparison of our method and state-of-the-art approaches on the Norman additive split.

surements of cellular responses to gene perturbations (Dixit et al., 2016; Jaitin et al., 2016; Datlinger et al., 2017). However, the combinatorial explosion of possible perturbation conditions makes exhaustive experiments infeasible, motivating the development of accurate and generalizable *in silico* perturbation prediction models.

A fundamental biological characteristic of perturbation responses is that they are rarely gene-independent (Dixit et al., 2016). In practice, genetic perturbations induce structured, program-level transcriptional responses (Subramanian et al., 2005), in which groups of functionally related genes (often corresponding to biological pathways such as cell-cycle regulation or stress response) are co-regulated to execute specific cellular processes. Particularly, these modular responses are pronounced in differentially expressed genes and under combinatorial perturbations (Norman et al., 2019), where interactions between gene programs, rather than isolated genes, govern cellular outcomes. Accurately modeling these coordinated, module-level behaviors is therefore essential for robust perturbation prediction.

Although recent approaches have made substantial progress (Lotfollahi et al., 2019; Wu et al., 2022), they do not explicitly model coordinated program-level responses

[†]Corresponding author.

in gene perturbation prediction. This limitation arises from two complementary factors. **i) Gene-wise modeling neglects program-level coordination.** Many foundation and dynamic generative models (Cui et al., 2024; Hao et al., 2024; Yang et al., 2024; Zeng et al., 2025; Chi et al., 2025a; Klein et al., 2025) represent gene expression in a flat, gene-wise manner or compress it into unstructured latent spaces. While effective for modeling marginal gene expression, such representations lack explicit mechanisms to capture coordination among groups of functionally related genes, making it difficult to model program-level transcriptional responses. **ii) Static biological priors cannot capture dynamic program coordination.** Graph-based approaches (Kamimoto et al., 2023; Bereket & Karaletsos, 2023; Roohani et al., 2024; Chi et al., 2025b) attempt to incorporate gene relations through predefined priors such as Gene Ontology (Consortium, 2004), protein–protein interaction networks (Szklarczyk et al., 2019), or gene regulatory graphs (Karlebach & Shamir, 2008). However, these priors are typically static, incomplete, and context-agnostic, limiting their ability to model the dynamic reorganization and coordination of gene programs across different cell types and perturbation conditions (Milano et al., 2022).

To address these challenges, a perturbation model should both induce gene programs beyond flat gene-wise representations and model their coordinated interactions in a context-adaptive manner, without relying on fixed biological graphs. Building on this insight, we propose **scBIG**, a module-inductive perturbation prediction framework designed to explicitly model coordinated gene programs. scBIG addresses the aforementioned challenges through a three-stage design of (module induction, structured generative modeling, structure-aware alignment). **i) Gene-Relation Clustering (GRC) (§2.1).** To move beyond flat gene-wise representations, scBIG first induces biologically coherent gene programs directly from data. GRC adaptively partitions genes into functional modules by integrating semantic embeddings from pretrained foundation models with high-confidence protein–protein interaction priors, providing a program-level inductive scaffold. **ii) Gene-Cluster-Aware Encoder (GCAE) and Conditional Flow Matching (§2.2, §2.3).** Building on the induced programs, we introduce a hierarchical GCAE that explicitly models high-order interactions among gene programs, enabling structured reasoning beyond independent genes. These structured representations are then modeled within a *conditional flow matching* framework, which serves as a flexible generative backbone for perturbation response prediction. **iii) Structure-Aware Alignment (§2.4).** To ensure that induced program coordination is preserved during generation, we further introduce a structure-aware alignment mechanism comprising *Cluster Correlation Alignment* and *Pathway-informed Optimal Transport*. These objectives enforce consistency at both

the module and pathway levels, encouraging biologically coherent and coordinated transcriptional responses.

Extensive experiments on multiple single-cell perturbation benchmarks demonstrate that scBIG consistently outperforms state-of-the-art methods, particularly on unseen and combinatorial perturbation settings, *e.g.*, it surpasses 13 leading methods, delivering an average performance gain of 6.7% over the best-performing baselines on key metrics.

Our main contributions are summarized as follows:

- To the best of our knowledge, this work is among the first to explicitly formalize a *module-level* inductive bias for *generative* perturbation prediction, moving beyond unstructured gene-wise modeling toward coordinated functional programs.
- We present **scBIG**, a module-inductive framework that induces gene programs from data (via GRC), performs hierarchical reasoning over inter-program interactions (via a GCAE), and enforces structure-preserving objectives to maintain biological coherence during generation (via Structure-Aware Alignment).
- Extensive evaluations on multiple single-cell perturbation benchmarks show that scBIG consistently outperforms 13 strong baselines, with particularly large gains on out-of-distribution generalization and combinatorial perturbation settings.

2. Method

Overview. As shown in Fig. 2, scBIG is a module-inductive generative framework for predicting transcriptional responses to genetic perturbations with high structural fidelity. It is designed to explicitly capture program structure and preserve coordinated responses during generation. The framework consists of three components. These components work in a complementary manner, from inducing gene modules to generating and aligning structure-consistent perturbation responses. (i) Gene-Relation Clustering (§2.1) adaptively partitions the gene space into biologically coherent modules by fusing foundation-model semantics with high-confidence PPI priors. (ii) Generative Modeling via GCAE(§2.2) uses a Gene-Cluster-Aware Encoder to capture inter-module dependencies and produce structured latent representations for a conditional flow-matching backbone (§2.3). (iii) Structure-Aware Alignment (§2.4) enforces biological consistency via *Cluster Correlation Alignment* and *Pathway-informed Optimal Transport*.

Together, these components yield predictions that are accurate at the expression level while preserving coordinated, program-level structure. Implementation details, including default hyperparameter settings and full algorithmic procedures, are provided in §A.3.1.

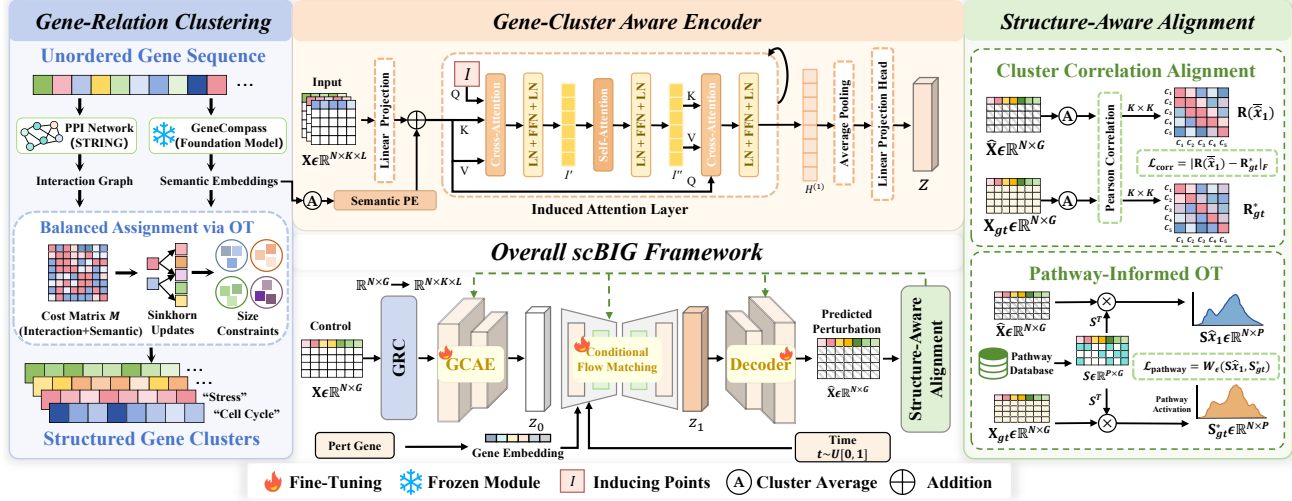


Figure 2. Overview of the scBIG framework. (§2) (Left) **Gene-Relation Clustering** (GRC) partitions the unordered gene space into K biologically coherent modules via optimal transport, integrating semantic embeddings from foundation models with high-confidence PPI priors. (Middle) **Generative Backbone**. The framework encodes cells using the **Gene-Cluster-Aware Encoder** (GCAE), which captures high-order inter-module interactions through a bottleneck attention mechanism with inducing points (Top). These latent representations guide a **Conditional Flow Matching** module (Bottom) to model the continuous transition from control (z_0) to perturbed (z_1) states. (Right) **Structure-Aware Alignment**. To ensure phenotypic fidelity, the entire pipeline is jointly optimized with two structural regularizers: **Cluster Correlation Alignment**, which preserves module-level co-expression patterns, and **Pathway-informed Optimal Transport**, which aligns predicted responses with canonical biological pathways.

2.1. Gene-Relation Clustering (GRC)

The unordered and high-dimensional nature of single-cell gene expression data presents a significant challenge for revealing meaningful regulatory structures. To introduce a structured inductive bias, we first partition the G genes into K functionally coherent clusters, $\mathcal{C} = \{c_1, \dots, c_K\}$, capturing both semantic similarity and biological interactions.

Integrating Semantic and Biological Priors. Our Gene-Relation Clustering (GRC) approach constructs this gene partition by solving a balanced assignment problem using Optimal Transport (OT). This framework integrates two complementary priors: First, the semantic representation of genes is derived from a pre-trained foundation model (e.g., GeneCompass (Yang et al., 2024)). Specifically, we obtain a gene embedding matrix $\mathbf{E} = [E_1, \dots, E_G]^\top \in \mathbb{R}^{G \times d}$, where each gene embedding E_i encodes co-expression patterns and context-specific regulatory information. Second, a binary Protein-Protein Interaction (PPI) adjacency matrix $\mathbf{A}^{\text{PPI}} \in \{0, 1\}^{G \times G}$ is constructed by thresholding interaction scores from the STRING (Szklarczyk et al., 2019) database at 700 to retain high-confidence interactions.

Cost Matrix Formulation. To jointly leverage these two priors, we define cluster centroids $\{\mu_k\}_{k=1}^K$ in the semantic space, and construct a combined cost matrix $\mathbf{C} \in \mathbb{R}^{G \times K}$, where each entry is computed as:

$$C_{ik} = D^{\text{sem}}(E_i, \mu_k) + D^{\text{PPI}}(i, k), \quad (1)$$

where $D^{\text{sem}}(E_i, \mu_k) = 1 - \text{cosine}(E_i, \mu_k)$ measures the

semantic dissimilarity between gene i and cluster k , and $D^{\text{PPI}}(i, k) = 1 - \frac{1}{|c_k|} \sum_{j \in c_k} A_{ij}^{\text{PPI}}$ penalizes low PPI coherence within cluster k .

Balanced Assignment via Optimal Transport. We solve the assignment problem by minimizing the transport cost $\langle \Pi, \mathbf{C} \rangle$ subject to uniform marginal constraints $a = \frac{1}{G} \mathbf{1}_G$ and $b = \frac{1}{K} \mathbf{1}_K$. This OT formulation imposes an approximately balanced soft assignment. To handle the dependency of D^{PPI} on cluster membership, GRC is solved *offline* through an alternating optimization: we update the transport plan Π via the Sinkhorn algorithm, followed by a capacity-constrained rounding step to ensure a strictly balanced hard partition (i.e., $|c_k| = G/K$).

Module-Structured Input Construction. Each gene is assigned to cluster $k_i = \arg \max_k \Pi_{ik}^*$. The resulting clusters are fixed to reorder the raw data $\mathbf{X} \in \mathbb{R}^{N \times G}$ into a structured representation $\mathbf{X} \in \mathbb{R}^{N \times K \times L}$, where $L = G/K$. This transformation provides the hierarchical input necessary for downstream inter-module modeling.

2.2. Gene-Cluster Aware Encoder (GCAE)

To bridge high-resolution transcriptomics with structured modules, GCAE operates on K gene clusters defined by GRC. For each cluster k , we derive a comprehensive module representation $\mathbf{h}_k^{(0)} \in \mathbb{R}^D$ through a dual-stream fusion:

$$\mathbf{h}_k^{(0)} = \text{Proj}_{\text{exp}}(\mathbf{x}_{c_k}) + \text{Proj}_{\text{sem}}\left(\frac{1}{|c_k|} \sum_{g \in c_k} E_g\right), \quad (2)$$

where $\mathbf{x}_{c_k} \in \mathbb{R}^L$ (with $L = G/K$) is the raw expression vector of genes in cluster k , and E_g are pre-trained foundation model embeddings. This design projects both local expression patterns and global semantic priors into a shared D -dimensional latent space. The resulting $\mathbf{H}^{(0)} \in \mathbb{R}^{K \times D}$ is augmented with relational position encodings as the input for inter-module modeling.

Inter-Module Modeling via Latent Bottleneck. To capture regulatory dependencies, GCAE employs a Perceiver-style bottleneck (Jaegle et al., 2021) with M learnable *Inducing Points* $\mathbf{I} \in \mathbb{R}^{M \times D}$ ($M < K$). The encoding follows a “Compress-Process-Broadcast” paradigm:

$$\begin{aligned}\mathbf{I}' &= \text{LN}(\mathbf{I} + \text{CrossAttn}(\mathbf{I}, \mathbf{H}^{(0)})), \\ \mathbf{I}'' &= \text{LN}(\mathbf{I}' + \text{SelfAttn}(\mathbf{I}')), \\ \mathbf{H}^{(1)} &= \text{LN}(\mathbf{H}^{(0)} + \text{CrossAttn}(\mathbf{H}^{(0)}, \mathbf{I}'')),\end{aligned}\quad (3)$$

where \mathbf{I}' aggregates information from all modules, \mathbf{I}'' captures global latent interactions, and $\mathbf{H}^{(1)}$ represents the updated cellular state.

$$\mathbf{Z} = \text{Linear} \left(\frac{1}{K} \sum_{k=1}^K \mathbf{H}_k^{(1)} \right), \quad (4)$$

where $\mathbf{Z} \in \mathbb{R}^D$ is the final latent embedding utilized for perturbation flow matching and reconstruction. This design ensures that the cell-level representation encapsulates the collaborative dynamics of all functional gene modules.

Latent Manifold Pre-training. The encoder-decoder pair is pre-trained via reconstruction to ensure a robust latent manifold. Specifically, we use a reconstruction loss defined as:

$$\mathcal{L}_{\text{recon}} = \frac{1}{N} \sum_{i=1}^N \|\hat{\mathbf{x}}_i - \mathbf{x}_i\|_2^2, \quad (5)$$

where \mathbf{x}_i represents the i -th input expression vector from the batch, and $\hat{\mathbf{x}}_i$ is the corresponding reconstructed expression vector. This loss encourages the model to learn a meaningful and robust latent representation of the input gene expression data.

2.3. Conditional Flow Matching Backbone

Perturbation Vector Field Regression. We formalize perturbation prediction as learning a conditional probability path between the latent states of control and perturbed cells. Let $\mathbf{z}_0 = \text{GCAE}(\mathbf{x}_{\text{ctrl}})$ and $\mathbf{z}_1 = \text{GCAE}(\mathbf{x}_{\text{pert}})$ denote the latent embeddings of unperturbed and perturbed cells, respectively, as derived from the pre-trained encoder. We define a time-varying vector field $v_\theta(\mathbf{z}_t, t, \mathbf{c})$ parameterized by a neural network, where \mathbf{c} encodes the perturbation via ESM2 (Lin et al., 2023) embeddings. The model is trained to regress the vector field:

$$\mathcal{L}_{\text{flow}} = \mathbb{E}_{t, \mathbf{z}_0, \mathbf{z}_1} \|v_\theta(\mathbf{z}_t, t, \mathbf{c}) - (\mathbf{z}_1 - \mathbf{z}_0)\|^2, \quad (6)$$

where $\mathbf{z}_t = (1 - t)\mathbf{z}_0 + t\mathbf{z}_1$ is the interpolation path.

To ensure the decoded expression $\hat{\mathbf{x}}_1 = \text{Dec}(\hat{\mathbf{z}}_1)$ adheres to biological priors, we introduce two structured consistency objectives through the differentiable encode-flow-decode pipeline.

2.4. Structure-Aware Alignment Objectives

Cluster Correlation Alignment. To preserve the functional co-expression patterns between gene modules, we constrain the inter-cluster correlation structure of the predicted expression profile. Specifically, let $\mathbf{R}(\hat{\mathbf{x}}_1) \in \mathbb{R}^{K \times K}$ be the Pearson correlation matrix of the cluster-aggregated expressions. We then align it with the ground truth via the loss:

$$\mathcal{L}_{\text{corr}} = \|\mathbf{R}(\hat{\mathbf{x}}_1) - \mathbf{R}_{gt}^*\|_F, \quad (7)$$

where \mathbf{R}_{gt}^* is the precomputed target correlation for perturbation p . This constrains the model to capture higher-order regulatory dependencies between gene modules.

Pathway-informed Optimal Transport. To enforce phenotypic validity, we match the distribution of predicted pathway activations to the ground truth. Specifically, we leverage a pathway membership matrix $\mathbf{S} \in \{0, 1\}^{P \times G}$ mapping G genes to P pre-defined biological pathways from Reactome database (Fabregat et al., 2018). We then compute the Sinkhorn distance in the pathway-quotient space:

$$\mathcal{L}_{\text{pathway}} = \mathcal{W}_\epsilon(\mathbf{S}\hat{\mathbf{x}}_1, \mathbf{S}_{gt}^*), \quad (8)$$

where \mathbf{S}_{gt}^* denotes target activations. This ensures the generated cells lie within biologically plausible manifolds.

The total objective is:

$$\mathcal{L} = \mathcal{L}_{\text{flow}} + \lambda_{\text{corr}} \mathcal{L}_{\text{corr}} + \lambda_{\text{pathway}} \mathcal{L}_{\text{pathway}}, \quad (9)$$

optimized end-to-end with target statistics cached for efficiency.

3. Experiments

3.1. Experimental Setup

Datasets and Scenarios. We evaluate **scBIG** on two widely recognized benchmarks: Norman (Norman et al., 2019) and Replogle2022_rpe1 (Replogle et al., 2022). We consider two settings. **(i) Additive setting:** we evaluate on *unseen dual-gene* perturbations formed by pairing two genes that are each observed in training, testing combinatorial generalization via composition. **(ii) Holdout setting:** we hold out a subset of genes entirely from training and evaluate zero-shot on perturbations involving these unseen genes, including *unseen single-gene* and *unseen dual-gene* (two unseen genes) cases. Further details on data processing and split construction are provided in §A.3.

Table 1. Comparison of different methods across evaluation metrics on the Norman additive split (§3.2); Type abbreviations: Sta.=Statistical, Found.=Foundation, Gra.=Graph-based, Gen.=Generative.

Type	Method	Public	$\rho\Delta \uparrow$	$\rho\Delta^D \uparrow$	$ACC\Delta \uparrow$	$ACC\Delta^D \uparrow$	$DES \uparrow$	$PDS \uparrow$	$L2 \downarrow$	$MSE \downarrow$	$MAE \downarrow$
Sta.	Control	—	—	—	—	—	0.5000	9.25	0.0487	0.1720	
	Linear	—	0.6211	0.7075	0.8007	0.8906	0.3192	0.5363	6.76	0.0265	0.1233
	Linear-scGPT (Ahlmann-Eltze et al., 2025)	<i>Nature Methods</i> '25	0.6925	0.7514	0.8424	0.9688	0.5023	0.7913	5.31	0.0155	0.0942
Found.	scGPT (Cui et al., 2024)	<i>Nature Methods</i> '24	0.4408	0.4416	0.8125	0.4839	0.2504	0.5022	7.35	0.0296	0.1285
	scFoundation (Hao et al., 2024)	<i>Nature Methods</i> '24	0.6813	0.4778	0.8768	0.7453	0.5409	0.7994	4.91	0.0138	0.0852
	GeneCompass (Yang et al., 2024)	<i>Cell Research</i> '24	0.6897	0.4810	0.8916	0.7484	0.5948	0.8024	4.77	0.0124	0.0808
Gra.	CellFM (Zeng et al., 2025)	<i>Cell Research</i> '25	0.5947	0.5209	0.8819	0.8459	0.7550	0.7419	5.41	0.0161	0.0889
	GEARS (Roohani et al., 2024)	<i>Nat. Biotechnol.</i> '23	0.7134	0.5065	0.8916	0.7641	0.6220	0.8155	4.59	0.0117	0.0788
	CellOracle (Kamimoto et al., 2023)	<i>Nature</i> '23	0.0437	0.2567	0.4942	0.4536	0.0319	0.5277	11.1	0.0691	0.2001
Gen.	GraphVCI (Bereket & Karaletsos, 2023)	<i>ICLR</i> '23	0.5468	0.5722	0.8034	0.7905	0.6495	0.5151	6.68	0.0258	0.1177
	samsVAE (Wu et al., 2022)	<i>NeurIPS</i> '23	0.6497	0.7750	0.8470	0.9658	0.6138	0.6689	6.87	0.0329	0.1067
	STATE (Adduri et al., 2025)	<i>bioRxiv</i> '25	0.2439	0.2628	0.8023	0.4141	0.4891	0.5171	9.02	0.0421	0.1343
	CellFlow (Klein et al., 2025)	<i>bioRxiv</i> '25	0.7892	0.7275	0.9151	0.9391	0.8113	0.7581	4.54	0.0114	0.0775
Gen.	scBIG (Ours)	<i>Proposed</i>	0.8496	0.8230	0.9197	0.9906	0.8593	0.8548	3.92	0.0091	0.0689

Comparison Baselines. We systematically compare **scBIG** against 13 state-of-the-art baselines across four paradigms: (1) **Foundation Models**, including **scGPT** (Cui et al., 2024), **scFoundation** (Hao et al., 2024), **GeneCompass** (Yang et al., 2024), and **CellFM** (Zeng et al., 2025); (2) **Graph-based Models**, such as **GEARS** (Roohani et al., 2024), **CellOracle** (Kamimoto et al., 2023), and **GraphVCI** (Bereket & Karaletsos, 2023); (3) **Generative Models** that operate in latent spaces, including **samsVAE** (Wu et al., 2022), **STATE** (Adduri et al., 2025), and **CellFlow** (Klein et al., 2025); and (4) **Statistical Methods**, comprising **Control**, **Linear**, and **Linear-scGPT** (Ahlmann-Eltze et al., 2025).

3.2. Benchmarking Performance on the Norman Dataset

Additive Split. As summarized in Table 1, **scBIG** establishes a new state-of-the-art across all evaluated metrics. Beyond achieving the lowest absolute errors in terms of L2, MSE, and MAE, our framework demonstrates a superior ability to capture perturbation-induced distributional shifts. Specifically, **scBIG** surpasses the advanced baseline **CellFlow** by **7.7%** on $\rho\Delta$ and **GeneCompass** by **6.5%** on PDS. Furthermore, the **5.9%** improvement over **CellFlow** on the DES metric underscores our model’s precision in identifying differentially expressed genes (DEGs), validating the efficacy of our module-level inductive bias for predicting unseen combinatorial effects.

Holdout Split. Table 2 highlights the substantial advantages of **scBIG** in extrapolating to entirely unseen perturbations. On the unseen single-perturbation task, our method achieves significant relative gains over **CellFlow**, notably **38.0%** on $\rho\Delta^D$ and **12.4%** on PDS. In the even more challenging unseen double-perturbation task, while **Linear-scGPT** achieves competitive MSE, it does so at the expense of biological fidelity and DEG-specific accuracy. In contrast, **scBIG** outperforms **Linear-scGPT** by a wide margin—**20.6%** on $\rho\Delta^D$ and **35.9%** on DES. These results collectively affirm that our module-structured representa-

tions better preserve the functional gene programs that are often lost in global error-minimization approaches.

3.3. Validation on the RPE1 Dataset

As demonstrated in Table 3, **scBIG** establishes a new state-of-the-art on the RPE1 dataset, confirming that its advantages generalize to diverse cellular contexts beyond the K562 cell line. Our framework significantly outperforms all competing methods across nearly every metric. Notably, **scBIG** surpasses the previous leading method, **CellFlow**, by 25.7% on $\rho\Delta$ and 34.9% on $\rho\Delta^D$, showcasing its superior ability to capture both global expression changes and key DEG-specific effects. This enhanced precision is further evidenced by a 1.5% improvement in PDS and top scores in $ACC\Delta$ and $ACC\Delta^D$. Moreover, our model consistently minimizes prediction error, reducing L2, MSE, and MAE by 5.6%, 12.6%, and 4.9% respectively, relative to **CellFlow**. Collectively, these results validate that the biological structure incorporated into **scBIG** provides a robust and applicable inductive bias for gene perturbation modeling.

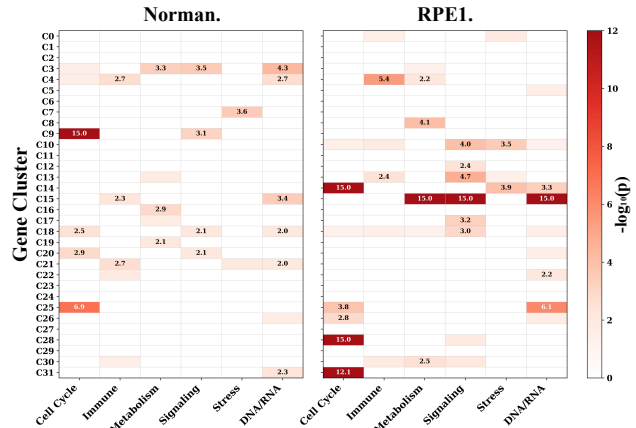


Figure 3. Functional enrichment analysis of GRC gene clusters across two datasets (§3.4).

Table 2. Comparison of different methods across evaluation metrics on the Norman holdout split (§3.2); Type abbreviations: Sta.=Statistical, Found.=Foundation, Gra.=Graph-based, Gen.=Generative.

Type	Method	Public	$\rho\Delta \uparrow$	$\rho\Delta^D \uparrow$	$ACC\Delta \uparrow$	$ACC\Delta^D \uparrow$	$DES \uparrow$	$PDS \uparrow$	$L2 \downarrow$	$MSE \downarrow$	$MAE \downarrow$
<i>Single Gene Perturbation</i>											
Sta.	Control	—	—	—	—	—	0.5000	4.33	0.0108	0.0685	
Sta.	Linear	—	0.5924	0.6021	0.7695	0.8476	0.4548	0.5119	3.46	0.0067	0.0516
Sta.	Linear-scGPT (Ahlmann-Eltze et al., 2025)	<i>Nature Methods</i> '25	0.6072	0.6352	0.7620	0.8095	0.4584	0.6571	3.60	0.0072	0.0575
Found.	scGPT (Cui et al., 2024)	<i>Nature Methods</i> '24	0.5172	0.5358	0.7509	0.8286	0.5987	0.5048	3.58	0.0071	0.0530
Found.	scFoundation (Hao et al., 2024)	<i>Nature Methods</i> '24	0.4453	0.3144	0.6882	0.7429	0.3897	0.6619	3.65	0.0079	0.0568
Found.	GeneCompass (Yang et al., 2024)	<i>Cell Research</i> '24	0.5307	0.3423	0.7006	0.7429	0.4543	0.5857	3.44	0.0066	0.0546
Found.	CellFM (Zeng et al., 2025)	<i>Cell Research</i> '25	0.4331	0.5226	0.6708	0.7119	0.5318	0.5524	3.83	0.0086	0.0600
Gra.	GEARS (Roohani et al., 2024)	<i>Nat. Biotechnol.</i> '23	0.4539	0.5345	0.7059	0.8024	0.3968	0.4905	3.77	0.0078	0.0574
Gra.	GraphVCI (Bereket & Karaletsos, 2023)	<i>ICLR</i> '23	0.3902	0.1865	0.7054	0.5583	0.1395	0.5000	3.28	0.0066	0.0500
Gen.	samsVAE (Wu et al., 2022)	<i>NeurIPS</i> '23	0.4778	0.4982	0.7050	0.8310	0.3366	0.3452	3.88	0.0081	0.0614
Gen.	STATE (Adduri et al., 2025)	<i>bioRxiv</i> '25	0.3085	0.5207	0.7600	0.5763	0.5712	0.5048	5.94	0.0177	0.0737
Gen.	CellFlow (Klein et al., 2025)	<i>bioRxiv</i> '25	0.5930	0.4736	0.7778	0.8119	0.6280	0.6643	3.40	0.0076	0.0535
Gen.	scBIG (Ours)	<i>Proposed</i>	0.6507	0.6537	0.7876	0.8548	0.6333	0.7467	3.26	0.0065	0.0491
<i>Double Genes Perturbation</i>											
Sta.	Control	—	—	—	—	—	0.5000	6.02	0.0200	0.0984	
Sta.	Linear	—	0.7179	0.8277	0.8240	0.9200	0.5637	0.5000	4.31	0.0105	0.0656
Sta.	Linear-scGPT (Ahlmann-Eltze et al., 2025)	<i>Nature Methods</i> '25	0.7351	0.7230	0.8282	0.9100	0.6118	0.7000	3.91	0.0080	0.0626
Found.	scGPT (Cui et al., 2024)	<i>Nature Methods</i> '24	0.6350	0.4719	0.8068	0.8333	0.4456	0.5000	4.70	0.0124	0.0726
Found.	scFoundation (Hao et al., 2024)	<i>Nature Methods</i> '24	0.6605	0.4445	0.7964	0.9200	0.6538	0.6500	3.91	0.0083	0.0589
Found.	GeneCompass (Yang et al., 2024)	<i>Cell Research</i> '24	0.6437	0.6866	0.7471	0.7400	0.5905	0.6000	4.37	0.0108	0.0723
Found.	CellFM (Zeng et al., 2025)	<i>Cell Research</i> '25	0.5615	0.8151	0.7072	0.7600	0.6746	0.5000	4.89	0.0132	0.0804
Gra.	GEARS (Roohani et al., 2024)	<i>Nat. Biotechnol.</i> '23	0.5087	0.6578	0.7130	0.8300	0.4156	0.5000	5.00	0.0138	0.0788
Gra.	GraphVCI (Bereket & Karaletsos, 2023)	<i>ICLR</i> '23	0.4290	0.5429	0.6889	0.6533	0.4003	0.5048	4.61	0.0114	0.0725
Gen.	samsVAE (Wu et al., 2022)	<i>NeurIPS</i> '23	0.6267	0.6402	0.7539	0.8800	0.5183	0.6500	4.66	0.0118	0.0742
Gen.	STATE (Adduri et al., 2025)	<i>bioRxiv</i> '25	0.3786	0.6379	0.8126	0.5800	0.7097	0.5000	5.94	0.0177	0.0737
Gen.	CellFlow (Klein et al., 2025)	<i>bioRxiv</i> '25	0.7404	0.6774	0.8388	0.8400	0.7636	0.4500	4.12	0.0097	0.0621
Gen.	scBIG (Ours)	<i>Proposed</i>	0.8026	0.8719	0.8552	0.9700	0.8313	0.7440	3.68	0.0083	0.0554

3.4. Biological Analysis of Gene Clusters

Functional Relevance of GRC Gene Modules. To validate the biological significance of the partitions generated by GRC, we performed pathway enrichment analysis on the 32 gene modules using the Reactome database (Fabregat et al., 2018). As shown in Fig. 3, GRC effectively groups genes into functionally coherent modules across both datasets. In the Norman dataset, Cluster 9 and Cluster 3 are significantly enriched in *Cell Cycle* and *DNA/RNA-related* pathways, respectively. In the larger RPE1 dataset, these patterns become even more pronounced: Cluster 14 exhibits high specificity for *Cell Cycle*, while Cluster 15 serves as a functional hub for *Metabolism* and *Signaling*. These results confirm that GRC reliably identifies gene modules that mirror established biological hierarchies. Detailed enrichment results for specific subpathways are provided in §A.5.

Mechanistic Insights via Attention Shifts. We further investigated whether GCAE leverages these modules to capture regulatory dependencies. Fig. 4 visualizes the attention shift (Δ Attention) relative to the control condition for two representative perturbations in RPE1. For *NOL8* knockdown (a nucleolar protein essential for ribosome biogenesis), the model’s attention to Cluster 8 (enriched in *mTORC1 Signaling* and *Metabolism*) surged by approximately 29%, aligning with the known mechanism where impaired ribosome assembly triggers mTORC1 pathway dysregulation. Conversely, knockdown of *KCTD10*—a reg-

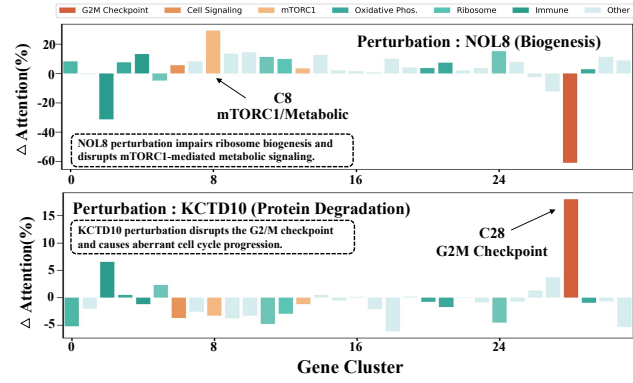


Figure 4. Differential attention (Δ Attention) across gene modules for two representative perturbations in RPE1. dataset(§3.4).

ulator of cullin-RING ligase complexes—induced an 18% increase in attention toward Cluster 28 (*G2/M Checkpoint*), consistent with its role in cell-cycle progression. These case studies demonstrate that **scBIG** moves beyond black-box prediction to capture the underlying biological mechanisms of gene regulation.

3.5. Ablation Study

Effectiveness of specific modules. Table 4a summarizes the ablation results for different clustering and encoding strategies under the Norman additive setting. With the GCAE encoder fixed, **GRC** clustering outperforms balanced

Table 3. Comparison of different methods across evaluation metrics on the RPE1 cell line (§3.3); Type abbreviations: Sta.=Statistical, Found.=Foundation, Gra.=Graph-based, Gen.=Generative.

Type	Method	Public	$\rho\Delta \uparrow$	$\rho\Delta^D \uparrow$	$ACC\Delta \uparrow$	$ACC\Delta^D \uparrow$	$DES \uparrow$	$PDS \uparrow$	$L2 \downarrow$	$MSE \downarrow$	$MAE \downarrow$
Sta.	Control	—	—	—	—	—	0.5000	7.03	0.0171	0.0768	
	Linear	—	0.2720	0.3630	0.5816	0.6919	0.2149	0.5318	14.13	0.0916	0.1491
	Linear-scGPT (Ahlmann-Eltze et al., 2025)	<i>Nature Methods</i> ’25	0.3404	0.5438	0.5852	0.7681	0.2497	0.5338	7.60	0.0172	0.0890
Found.	scGPT (Cui et al., 2024)	<i>Nature Methods</i> ’24	0.2840	0.5691	0.5882	0.7759	0.2980	0.5001	9.49	0.0246	0.1037
	scFoundation (Hao et al., 2024)	<i>Nature Methods</i> ’24	0.2037	0.3632	0.5489	0.6908	0.2331	0.5098	7.07	0.0155	0.0812
	GeneCompass (Yang et al., 2024)	<i>Cell Research</i> ’24	0.3113	0.4299	0.5758	0.7148	0.2873	0.5038	7.18	0.0162	0.0822
	CellFM (Zeng et al., 2025)	<i>Cell Research</i> ’25	0.3060	0.4299	0.5733	0.7086	0.2819	0.5039	7.20	0.0163	0.0825
Gra.	GEARS (Roohani et al., 2024)	<i>Nat. Biotechnol.</i> ’23	0.3083	0.4289	0.5752	0.7096	0.2820	0.5004	7.18	0.0162	0.0822
	GraphVCI (Bereket & Karaletsos, 2023)	<i>ICLR</i> ’23	0.4294	0.5302	0.5589	0.6436	0.1863	0.5000	7.41	0.0157	0.0913
Gen.	samsVAE (Wu et al., 2022)	<i>NeurIPS</i> ’23	0.4083	0.5204	0.5998	0.7565	0.3280	0.4984	6.86	0.0140	0.0780
	STATE (Adduri et al., 2025)	<i>bioRxiv</i> ’25	0.3638	0.5298	0.6463	0.7891	0.3711	0.5011	8.38	0.0194	0.0759
	CellFlow (Klein et al., 2025)	<i>bioRxiv</i> ’25	0.3878	0.4391	0.6226	0.7194	0.3114	0.5441	6.48	0.0135	0.0711
	scBIG (Ours)	Proposed	0.4875	0.5925	0.6471	0.8089	0.5145	0.5520	6.12	0.0118	0.0676

K-means and the unordered baseline, yielding a **5.2%** and **1.5%** gain in $\rho\Delta$ and $ACC\Delta$, respectively. This underscores GRC’s superior ability to integrate functional similarities and PPI networks into precise module assignments. Furthermore, when GRC clustering is fixed, our GCAE significantly surpasses the standard Transformer, with $\rho\Delta$ and $ACC\Delta$ increasing by **1.8%** and **1.1%**. These results indicate that GCAE more effectively captures high-order inter-module dependencies.

Table 4b further ablates the **cluster balancing** strategy used in our chunk-wise perceiver attention. Unbalanced K-means forms highly skewed clusters (1–1812 genes per cluster), leading to attention dilution in large clusters and signal loss in small ones; while soft OT constraints partially mitigate this issue, our balanced OT clustering enforces near-uniform cluster sizes (~ 64 genes), ensuring equal attention capacity per chunk and preserving minority gene signals, which yields a **3.3%** improvement in $\rho\Delta^D$. Overall, the synergy between GRC and GCAE achieves the highest performance across all metrics, validating our structural design.

Effectiveness of biological regularization and constraints. As shown in Tables 4c and 4d, both biological losses are necessary and complementary. Using either $\mathcal{L}_{\text{corr}}$ or $\mathcal{L}_{\text{pathway}}$ alone yields moderate gains over the vanilla baseline, while jointly optimizing them achieves the best overall performance, with a **3.1%** improvement in $\rho\Delta$ and a **2.7%** gain in $\rho\Delta^D$. Notably, this trend holds across metrics, suggesting the two terms regularize distinct but complementary aspects of perturbation responses. Moreover, the weight sweep in Table 4d shows that over-emphasizing either term degrades accuracy—especially on strongly DE genes—whereas the optimum occurs when λ_{corr} and λ_{pathway} are balanced. This clearly indicates that correlation alignment and pathway-informed transport regularize the model at different granularities.

Impact of Gene Embeddings on Clustering and Perturbation Conditioning. We further evaluate how different gene embeddings affect GRC clustering quality. As shown

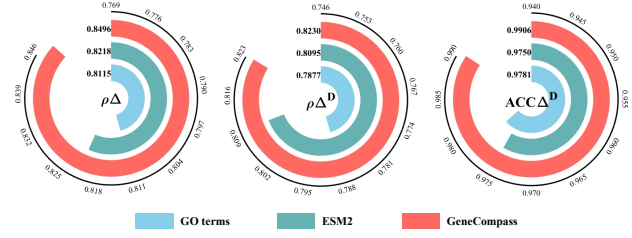


Figure 5. Comparison of Different Gene Embeddings for Clustering Performance Evaluation (§3.5).

in Fig. 5, *GeneCompass* consistently outperforms both *GO terms* (Consortium, 2004) and *ESM2* (Lin et al., 2023), especially on $\rho\Delta$ and $ACC\Delta^D$, suggesting that its context-aware semantics provide a stronger signal for forming biologically coherent modules. Interestingly, when the same embeddings are used for *perturbation condition injection* (Table 4e), *ESM2* becomes the stronger choice and achieves consistently better downstream scores than *GeneCompass*. We attribute this reversal to the nature of the learned representations: *GeneCompass* emphasizes gene–context dependencies that benefit module discovery, whereas *ESM2* encodes more fundamental functional priors that transfer more reliably to unseen perturbations, thereby improving out-of-distribution robustness in conditioning.

Finally, we report additional hyperparameter ablations and efficiency analyses in §A.1, and provide run-to-run standard deviations of evaluation metrics across multiple random seeds in §A.2.

4. Related Work

Single-cell Foundation Models. With the advancement of high-throughput sequencing technologies, large-scale single-cell scRNA-seq datasets have become widely available (Regev et al., 2017; Zheng et al., 2017). Recent foundation models, such as scGPT (Cui et al., 2024), scFoundation (Hao et al., 2024), GeneCompass (Yang et al., 2024), and CellFM (Zeng et al., 2025) leverage pretraining on mas-

Table 4. A set of ablative experiments on the Norman additive split (§3.5).

Cluster K-means	GRC	Encoding Normal GCAE	Norman Additive			
			$\rho\Delta$	$\rho\Delta^D$	ACC Δ	ACC Δ^D
✓	✓	✓	0.7781	0.7885	0.8849	0.9609
			0.8078	0.8109	0.9008	0.9625
	✓	✓	0.8239	0.8052	0.9059	0.9781
			0.8358	0.8190	0.9161	0.9813
	✓	✓	0.8348	0.8226	0.9097	0.9859
			0.8496	0.8230	0.9197	0.9906

(a) Clustering and encoding strategies.

Configuration	$\rho\Delta$	$\rho\Delta^D$	ACC Δ	ACC Δ^D
K-means Unbalanced	0.8249	0.7765	0.9163	0.9719
Soft Cluster ($\tau=0.5$)	0.8408	0.7923	0.9203	0.9797
Soft Cluster ($\tau=0.9$)	0.8411	0.7904	0.9200	0.9797
Ours	0.8496	0.8230	0.9197	0.9906

(b) Comparison of clustering strategies.

sive single-cell corpora to learn gene embeddings that capture rich co-expression patterns and contextual semantics, enabling strong performance on downstream tasks including batch correction and cell annotation. However, most of these models operate on a *flat* gene-token representation without an explicit program/module scaffold, and are not optimized to preserve coordinated program-level structure under perturbations. This design choice may limit their generalization in perturbation response prediction, particularly for unseen perturbations.

Generative Perturbation Modeling. Recent generative frameworks (Lotfollahi et al., 2019; Wu et al., 2022; Lotfollahi et al., 2023; Adduri et al., 2025) have shown strong performance in single-cell perturbation prediction by modeling response distributions and enabling extrapolation to unseen conditions. Unlasting (Chi et al., 2025a) and CellFlow (Klein et al., 2025) further improve distributional consistency by learning continuous transitions between control and perturbed states in a latent space, capturing smooth trajectories of gene-expression change. However, these models typically operate on flat gene-token representations or weakly structured latent bottlenecks and do not explicitly enforce *module-level coordination*. As a result, they may not preserve cross-program structure (e.g., module correlation patterns and pathway-level organization), which is critical for robust generalization under combinatorial and out-of-distribution perturbations.

Incorporating Biological Priors. A growing body of work enhances perturbation modeling by incorporating biological priors into the architecture (Chi et al., 2025b). GEARS (Roohani et al., 2024) integrates Gene Ontology (GO) (Consortium, 2004) and interaction-derived graphs via GNNs (Scarselli et al., 2008) to propagate signals across genes, while CellOracle (Kamimoto et al., 2023) leverages gene regulatory networks (GRNs) (Karlebach & Shamir, 2008) to simulate responses. These approaches improve interpretability by grounding predictions in structured biological knowledge. However, the effectiveness of such models often scales with the quality of the underlying graphs, which

$\mathcal{L}_{\text{corr}}$	$\mathcal{L}_{\text{pathway}}$	$\rho\Delta$	$\rho\Delta^D$	ACC Δ	ACC Δ^D
✓	✓	0.8242	0.8014	0.9076	0.9703
		0.8306	0.8146	0.9109	0.9859
		0.8361	0.8050	0.9164	0.9922

(c) Effectiveness of biological loss components.

λ_{corr}	λ_{pathway}	$\rho\Delta$	$\rho\Delta^D$	ACC Δ	ACC Δ^D
0.1	1.0	0.8437	0.7987	0.9179	0.9859
	0.1	0.8393	0.8162	0.9119	0.9891
	0.1	0.8496	0.8230	0.9197	0.9906

(d) Impact of loss weights.

Condition Embedding	$\rho\Delta$	$\rho\Delta^D$	ACC Δ	ACC Δ^D
GeneCompass	0.8397	0.8182	0.9164	0.9750
	0.8496	0.8230	0.9197	0.9906

(e) Comparison of gene embeddings for perturbed gene conditions.

may be subject to incomplete coverage, noise, or the inability to fully reflect dynamic, perturbation-induced regulatory rewiring (Milano et al., 2022). Consequently, there remains a critical need for strategies that can effectively bridge these static priors with broader, context-aware biological insights.

Compared with fixed graph propagation methods, our approach introduces a shift toward knowledge-augmented modularity. Instead of relying solely on potentially incomplete static neighborhoods, scBIG leverages the rich contextual semantics from single-cell foundation models to induce functional gene programs. This design choice enables a more comprehensive coverage of gene relationships that may be absent in traditional graphs, allowing the model to capture high-order, cross-program coordination. By fusing molecular priors with the deep semantic embeddings of foundation models, scBIG moves beyond the limitations of isolated gene tokens and static local propagation to a more robust, module-aware framework.

5. Conclusion

Regarding the challenge of generalizing perturbation prediction to unseen genes and combinatorial interventions, we present scBIG, a module-inductive generative framework for modeling transcriptional responses with high structural fidelity. Compared to approaches that operate on flat gene-wise representations or rely on static and incomplete biological graphs, scBIG has merits in: **i) knowledge-augmented module induction** that adaptively constructs biologically coherent gene programs by fusing foundation-model semantics with high-confidence PPI priors; **ii) module-aware generative modeling** that captures inter-program dependencies through a Gene-Cluster-Aware Encoder within a conditional flow-matching backbone; **iii) structure-aware objectives** that preserve coordinated program-level behavior by enforcing module correlation consistency and pathway-level alignment in generated profiles. Extensive experiments on two widely used benchmarks confirm the effectiveness and robustness of scBIG across diverse perturbation settings.

Impact Statement

This study strictly utilizes publicly available single-cell transcriptomic datasets in full compliance with their respective Data Use Agreements. Our analysis involves no personally identifiable information (PII) or sensitive patient metadata. As a computational framework for in silico hypothesis generation, our model is intended for research purposes and does not constitute a clinical diagnostic tool. While it holds potential for accelerating drug discovery, all predictions require rigorous in vitro and in vivo validation before any therapeutic application. We advocate for the responsible use of generative AI in biology and caution against interpreting model outputs without proper biological context.

References

Adduri, A. K., Gautam, D., Bevilacqua, B., Imran, A., Shah, R., Naghipourfar, M., Teyssier, N., Ilango, R., Nagaraj, S., Dong, M., et al. Predicting cellular responses to perturbation across diverse contexts with state. *BioRxiv*, pp. 2025–06, 2025.

Ahlmann-Eltze, C., Huber, W., and Anders, S. Deep-learning-based gene perturbation effect prediction does not yet outperform simple linear baselines. *Nature Methods*, 22(8):1657–1661, 2025.

Aibar, S., González-Blas, C. B., Moerman, T., Huynh-Thu, V. A., Imrichova, H., Hulselmans, G., Rambow, F., Marine, J.-C., Geurts, P., Aerts, J., et al. Scenic: single-cell regulatory network inference and clustering. *Nature methods*, 14(11):1083–1086, 2017.

Bereket, M. and Karaletsos, T. Modelling cellular perturbations with the sparse additive mechanism shift variational autoencoder. *Advances in Neural Information Processing Systems*, 36:1–12, 2023.

Bradbury, J., Frostig, R., Hawkins, P., Johnson, M. J., Leary, C., Maclaurin, D., Necula, G., Paszke, A., VanderPlas, J., Wanderman-Milne, S., et al. Jax: composable transformations of python+ numpy programs. 2018.

Chi, C., Xia, J., Huang, Y., Zhou, J., Li, S., Liu, Y., Yu, C., and Li, S. Z. Unlasting: Unpaired single-cell multi-perturbation estimation by dual conditional diffusion implicit bridges. *arXiv preprint arXiv:2506.21107*, 2025a.

Chi, C., Xia, J., Zhou, J., Cheng, J., Yu, C., and Li, S. Z. Grape: Heterogeneous graph representation learning for genetic perturbation with coding and non-coding biotype. *arXiv preprint arXiv:2505.03853*, 2025b.

Consortium, G. O. The gene ontology (go) database and informatics resource. *Nucleic acids research*, 32(suppl_1): D258–D261, 2004.

Cui, H., Wang, C., Maan, H., Pang, K., Luo, F., Duan, N., and Wang, B. scgpt: toward building a foundation model for single-cell multi-omics using generative ai. *Nature methods*, 21(8):1470–1480, 2024.

Datlinger, P., Rendeiro, A. F., Schmidl, C., Krausgruber, T., Traxler, P., Klughammer, J., Schuster, L. C., Kuchler, A., Alpar, D., and Bock, C. Pooled crispr screening with single-cell transcriptome readout. *Nature methods*, 14(3): 297–301, 2017.

Dixit, A., Parnas, O., Li, B., Chen, J., Fulco, C. P., Jerby-Arnon, L., Marjanovic, N. D., Dionne, D., Burks, T., Raychowdhury, R., et al. Perturb-seq: dissecting molecular circuits with scalable single-cell rna profiling of pooled genetic screens. *cell*, 167(7):1853–1866, 2016.

Fabregat, A., Jupe, S., Matthews, L., Sidiropoulos, K., Gillespie, M., Garapati, P., Haw, R., Jassal, B., Korninger, F., May, B., et al. The reactome pathway knowledgebase. *Nucleic acids research*, 46(D1):D649–D655, 2018.

Hao, M., Gong, J., Zeng, X., Liu, C., Guo, Y., Cheng, X., Wang, T., Ma, J., Zhang, X., and Song, L. Large-scale foundation model on single-cell transcriptomics. *Nature methods*, 21(8):1481–1491, 2024.

Jaegle, A., Gimeno, F., Brock, A., Vinyals, O., Zisserman, A., and Carreira, J. Perceiver: General perception with iterative attention. In *International conference on machine learning*, pp. 4651–4664. PMLR, 2021.

Jaitin, D. A., Weiner, A., Yofe, I., Lara-Astiaso, D., Keren-Shaul, H., David, E., Salame, T. M., Tanay, A., van Oude-naarden, A., and Amit, I. Dissecting immune circuits by linking crispr-pooled screens with single-cell rna-seq. *Cell*, 167(7):1883–1896, 2016.

Kamimoto, K., Stringa, B., Hoffmann, C. M., Jindal, K., Solnica-Krezel, L., and Morris, S. A. Dissecting cell identity via network inference and in silico gene perturbation. *Nature*, 614(7949):742–751, 2023.

Karlebach, G. and Shamir, R. Modelling and analysis of gene regulatory networks. *Nature reviews Molecular cell biology*, 9(10):770–780, 2008.

Kingma, D. P. Adam: A method for stochastic optimization. *arXiv preprint arXiv:1412.6980*, 2014.

Klein, D., Fleck, J. S., Bobrovskiy, D., Zimmermann, L., Becker, S., Palma, A., Dony, L., Tejada-Lapuerta, A., Huguet, G., Lin, H.-C., et al. Cellflow enables generative single-cell phenotype modeling with flow matching. *BioRxiv*, pp. 2025–04, 2025.

Lin, Z., Akin, H., Rao, R., Hie, B., Zhu, Z., Lu, W., Smetanin, N., Verkuil, R., Kabeli, O., Shmueli, Y., et al.

Evolutionary-scale prediction of atomic-level protein structure with a language model. *Science*, 379(6637):1123–1130, 2023.

Lotfollahi, M., Wolf, F. A., and Theis, F. J. scgen predicts single-cell perturbation responses. *Nature methods*, 16(8):715–721, 2019.

Lotfollahi, M., Klimovskaia Susmelj, A., De Donno, C., Hetzel, L., Ji, Y., Ibarra, I. L., Srivatsan, S. R., Naghipourfar, M., Daza, R. M., Martin, B., et al. Predicting cellular responses to complex perturbations in high-throughput screens. *Molecular systems biology*, 19(6):e11517, 2023.

Milano, M., Agapito, G., and Cannataro, M. Challenges and limitations of biological network analysis. *BioTech*, 11(3):24, 2022.

Norman, T. M., Horlbeck, M. A., Replogle, J. M., Ge, A. Y., Xu, A., Jost, M., Gilbert, L. A., and Weissman, J. S. Exploring genetic interaction manifolds constructed from rich single-cell phenotypes. *Science*, 365(6455):786–793, 2019.

Peidli, S., Green, T. D., Shen, C., Gross, T., Min, J., Garda, S., Yuan, B., Schumacher, L. J., Taylor-King, J. P., Marks, D. S., et al. scperturb: harmonized single-cell perturbation data. *Nature Methods*, 21(3):531–540, 2024.

Qi, X., Zhao, L., Tian, C., Li, Y., Chen, Z.-L., Huo, P., Chen, R., Liu, X., Wan, B., Yang, S., et al. Predicting transcriptional responses to novel chemical perturbations using deep generative model for drug discovery. *Nature Communications*, 15(1):9256, 2024.

Regev, A., Teichmann, S. A., Lander, E. S., Amit, I., Benoist, C., Birney, E., Bodenmiller, B., Campbell, P., Carninci, P., Clatworthy, M., et al. The human cell atlas. *elife*, 6:e27041, 2017.

Replogle, J. M., Saunders, R. A., Pogson, A. N., Hussmann, J. A., Lenail, A., Guna, A., Mascibroda, L., Wagner, E. J., Adelman, K., Lithwick-Yanai, G., et al. Mapping information-rich genotype-phenotype landscapes with genome-scale perturb-seq. *Cell*, 185(14):2559–2575, 2022.

Roohani, Y., Huang, K., and Leskovec, J. Predicting transcriptional outcomes of novel multigene perturbations with gears. *Nature Biotechnology*, 42(6):927–935, 2024.

Roohani, Y. H., Hua, T. J., Tung, P.-Y., Bounds, L. R., Yu, F. B., Dobin, A., Teyssier, N., Adduri, A., Woodrow, A., Plosky, B. S., et al. Virtual cell challenge: Toward a turing test for the virtual cell. *Cell*, 188(13):3370–3374, 2025.

Scarselli, F., Gori, M., Tsoi, A. C., Hagenbuchner, M., and Monfardini, G. The graph neural network model. *IEEE transactions on neural networks*, 20(1):61–80, 2008.

Subramanian, A., Tamayo, P., Mootha, V. K., Mukherjee, S., Ebert, B. L., Gillette, M. A., Paulovich, A., Pomeroy, S. L., Golub, T. R., Lander, E. S., et al. Gene set enrichment analysis: a knowledge-based approach for interpreting genome-wide expression profiles. *Proceedings of the National Academy of Sciences*, 102(43):15545–15550, 2005.

Szklarczyk, D., Gable, A. L., Lyon, D., Junge, A., Wyder, S., Huerta-Cepas, J., Simonovic, M., Doncheva, N. T., Morris, J. H., Bork, P., et al. String v11: protein–protein association networks with increased coverage, supporting functional discovery in genome-wide experimental datasets. *Nucleic acids research*, 47(D1):D607–D613, 2019.

Theodoris, C. V., Xiao, L., Chopra, A., Chaffin, M. D., Al Sayed, Z. R., Hill, M. C., Mantineo, H., Brydon, E. M., Zeng, Z., Liu, X. S., et al. Transfer learning enables predictions in network biology. *Nature*, 618(7965):616–624, 2023.

Wolf, F. A., Angerer, P., and Theis, F. J. Scanpy: large-scale single-cell gene expression data analysis. *Genome biology*, 19(1):15, 2018.

Wu, Y., Barton, R. A., Wang, Z., Ioannidis, V. N., De Donno, C., Price, L. C., Voloch, L. F., and Karypis, G. Predicting cellular responses with variational causal inference and refined relational information. *arXiv preprint arXiv:2210.00116*, 2022.

Yang, X., Liu, G., Feng, G., Bu, D., Wang, P., Jiang, J., Chen, S., Yang, Q., Miao, H., Zhang, Y., et al. Genecompass: deciphering universal gene regulatory mechanisms with a knowledge-informed cross-species foundation model. *Cell Research*, 34(12):830–845, 2024.

Zeng, Y., Xie, J., Shangguan, N., Wei, Z., Li, W., Su, Y., Yang, S., Zhang, C., Zhang, J., Fang, N., et al. Cellfm: a large-scale foundation model pre-trained on transcriptomics of 100 million human cells. *Nature Communications*, 16(1):4679, 2025.

Zheng, G. X., Terry, J. M., Belgrader, P., Ryvkin, P., Bent, Z. W., Wilson, R., Ziraldo, S. B., Wheeler, T. D., McDermott, G. P., Zhu, J., et al. Massively parallel digital transcriptional profiling of single cells. *Nature communications*, 8(1):14049, 2017.

A. Appendix

The appendix is organized as follows:

- §A.1 offers more ablation experiments of scBIG, including analysis of key hyperparameters and efficiency.
- §A.2 shows the robustness of evalation on the Norman (Norman et al., 2019) dataset.
- §A.3 provides more implementation details of scBIG.
- §A.4 offers the detail of baseline methods.
- §A.5 analysis the pathway of gene clusters.
- §A.6 discusses the limitations and future work.

A.1. Ablation Study

A.1.1. IMPACT OF STRUCTURAL HYPERPARAMETERS.

Fig. 6 illustrates the model’s sensitivity to the number of clusters (K) and inducing points (M) under the Norman additive setting. We observe that a moderate structural constraint provides the optimal balance between model complexity and predictive fidelity. Specifically, reducing K from 128 to 32 consistently improves performance across all metrics, with the most robust results achieved at $K = 32$ and $M = 8$. These findings suggest that excessively fine-grained clustering may introduce noise, whereas a well-calibrated K effectively captures the functional modularity of gene regulation.

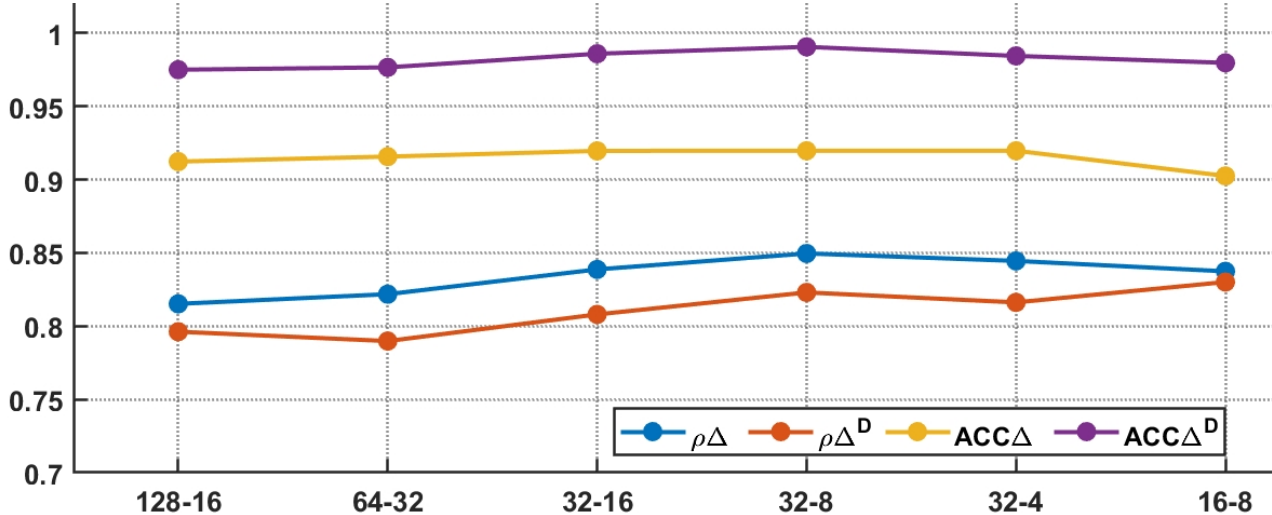


Figure 6. Performance of different configurations (Cluster number — Inducing points dimension) on various metrics.

A.1.2. EFFICIENCY ANALYSIS OF SCBIG

Table 5 presents the computational overhead incurred by our proposed biological consistency losses. We benchmark the per-step training time with a batch size of 1024 on a single NVIDIA RTX 3090 GPU. The baseline model, without biological losses, requires 83.17 ms per training step. Incorporating the cluster correlation loss $\mathcal{L}_{\text{corr}}$ results in 81.94 ms, while the pathway optimal transport loss $\mathcal{L}_{\text{pathway}}$ (incorporating 969 Reactome pathways and 100 Sinkhorn iterations) increases the step time to 87.91 ms. Integrating both losses yields 87.44 ms per step.

Notably, the addition of the cluster correlation loss alone shows a marginal reduction in training time (-1.23 ms) compared to the baseline. This phenomenon is likely attributed to two factors: (1) the computation of $\mathcal{L}_{\text{corr}}$ is highly efficient, involving only gene-to-cluster aggregation and a small 32×32 correlation matrix; and (2) JAX’s XLA compiler may identify more

efficient execution strategies when optimizing the augmented computational graph, as structural changes can trigger different kernel fusion opportunities. This observed variance falls within the expected measurement noise (std ≈ 1 ms).

In contrast, the pathway OT loss introduces a measurable overhead of approximately 4.7 ms (+5.7%), primarily due to the iterative Sinkhorn algorithm. The total overhead for both biological losses remains modest at approximately 5.1%, demonstrating that our biologically-informed objectives can be incorporated with minimal computational penalty.

Table 5. Computational overhead of biological consistency losses.

$\mathcal{L}_{\text{corr}}$	$\mathcal{L}_{\text{pathway}}$	Batch Size	Time/Step (ms)
✓	✓	1024	83.17
		1024	81.94
		1024	87.91
✓	✓	1024	87.44

Table 6 analyzes the computational overhead of pretrained encoder-decoder relative to the number of gene clusters K , which determines the granularity of our Gene-Cluster Aware Encoder (GCAE). With $K = 1$ (equivalent to global attention over all 2,051 genes), the model achieves a training time of 12.21 ms per step with a batch size of 256. As K increases, the cost grows due to the increased frequency of attention operations: $K = 32$ requires 29.91 ms, while $K = 512$ increases to 198.6 ms. In the extreme case of $K = 2,051$ (per-gene attention), memory constraints necessitate reducing the batch size to 128, resulting in 394.16 ms per step.

These results validate that our GCAE design with a moderate K (e.g., $K = 32$) provides an optimal trade-off between computational tractability and functional resolution. It maintains efficient throughput while enabling structured modeling of complex gene-gene interactions.

Table 6. Computational overhead of different gene cluster numbers.

K	Batch Size	Time/Step (ms)
1	256	12.2
16	256	22.4
32	256	29.9
128	256	65.2
512	256	198.6
2051	128	394.2

A.2. Robustness on the Norman dataset

To assess the stability of scBIG and its sensitivity to stochastic initialization, we conducted a rigorous robustness analysis across five independent trials. For each trial, the model was trained and evaluated using distinct random seeds, ensuring that the results are not artifacts of a specific initialization.

As summarized in Table 7 and Table 8, we report the standard deviation for each evaluation metric. The observed standard deviations remain consistently low across all tasks and data partitions, demonstrating that our module-inductive framework and flow-matching backbone are numerically stable.

Table 7. Standard deviation across five seeds on the Norman additive split.

Method	Public	$\rho\Delta$	$\rho\Delta^D$	$\text{ACC}\Delta$	$\text{ACC}\Delta^D$	DES	PDS	L2	MSE	MAE
GEARS	<i>Nat. Biotechnol.</i> '23	0.0055	0.0151	0.0031	0.0080	0.0081	0.0048	0.0649	0.0006	0.0014
scGPT	<i>Nature Methods</i> '24	0.0006	0.0045	0.0010	0.0010	0.0084	0.0026	0.0197	0.0002	0.0004
scFoundation	<i>Nature Methods</i> '24	0.0009	0.0031	0.0004	0.0036	0.0067	0.0029	0.0044	0.0001	0.0002
CellFlow	<i>bioRxiv</i> '25	0.0035	0.0146	0.0013	0.0213	0.0033	0.0074	0.0636	0.0004	0.0014
Ours	Proposed	0.0026	0.0038	0.0023	0.0029	0.0015	0.0096	0.0411	0.0002	0.0009

A.3. Experiments Setup

A.3.1. DEFAULT SETTINGS

Implementation Details. The scBIG framework was trained on a single NVIDIA RTX 3090 GPU using the JAX (Bradbury et al., 2018) deep learning framework with the Flax neural network library. Training consists of two stages: (1) encoder-decoder pretraining and (2) flow matching with biological consistency fine-tuning. The overall pipeline is summarized in Algorithms 1 to 3.

Before training, we obtain gene modules \mathcal{C} via Gene-Relation Clustering (GRC), as described in Algorithm 1.

Table 8. Standard deviation across five seeds on the Norman holdout split.

Method	Public	$\rho\Delta$	$\rho\Delta^D$	$ACC\Delta$	$ACC\Delta^D$	DES	PDS	L2	MSE	MAE
GEARS	<i>Nat. Biotechnol.'23</i>	0.0072	0.0122	0.0042	0.0091	0.0158	0.0023	0.0227	0.0001	0.0005
scGPT	<i>Nature Methods'24</i>	0.0008	0.0027	0.0003	0.0031	0.0155	0.0006	0.0039	0.0001	0.0001
scFoundation	<i>Nature Methods'24</i>	0.0072	0.0122	0.0042	0.0091	0.0158	0.0023	0.0227	0.0000	0.0005
CellFlow	<i>bioRxiv'25</i>	0.0026	0.0098	0.0013	0.0038	0.0042	0.0092	0.0053	0.0000	0.0001
Ours	<i>Proposed</i>	0.0016	0.0036	0.0021	0.0014	0.0042	0.0026	0.0105	0.0000	0.0002

Stage 1: Encoder-Decoder Pretraining. The GCAE encoder and decoder are jointly pretrained for 100 epochs using the Adam (Kingma, 2014) optimizer with a learning rate of 10^{-4} and batch size of 256. The encoder employs a Perceiver-style induced attention mechanism with 8 inducing points per gene module, reducing computational complexity from $O(G^2)$ to $O(G \cdot M)$ where G is the number of genes and M is the number of inducing points. The Stage I pretraining procedure is detailed in Algorithm 2.

Stage 2: Joint Flow Matching with Biological Consistency. In the second stage, the flow matching loss and biological consistency losses are **jointly optimized at every training step**. The conditional flow network is trained for 500,000 iterations with a batch size of 1024 (accumulated over 20 gradient steps). We use the Adam optimizer with gradient clipping (max norm 1.0) and a learning rate of 5×10^{-5} . The Stage II joint optimization procedure is detailed in Algorithm 3.

To solve the Ordinary Differential Equations (ODEs) during both training (for consistency losses) and inference, we follow the configuration of *CellFlow* (Klein et al., 2025).

Table 9. Experiment Configurations.

Category	Hyperparameter	Value
Model Settings	Latent dimension D	50
	Embedding dimension	256
	Encoder layers	3
	Attention heads	8
	Inducing points M	8
	Gene clusters K	32
	Flow hidden layers	2
	Flow hidden dimension	1024
	Flow dropout	0.1
	Condition embedding dim	256
Stage 1 Pretrain	Epochs	100
	Batch size	256
	Learning rate	10^{-4}
	Optimizer	Adam
Stage 2 Flow	Iterations	500,000
	Batch size B	1024
	Gradient accumulation	20
	Gradient clip norm	1.0
	Optimizer	Adam
	Learning rate	5×10^{-5}
	λ_{corr}	0.1
	$\lambda_{pathway}$	0.1

A.3.2. DATASET DETAILS

Transcriptomic profiles were sourced from the scPerturb resource (Peidli et al., 2024). To ensure robust downstream analysis, we implemented a rigorous preprocessing pipeline following the established Scanpy framework (Wolf et al., 2018):

- **Quality Control (QC):** We enforced stringent filtering criteria to eliminate low-quality cells and stochastic noise, specifically retaining cells with a minimum of 1,000 detected genes and genes expressed in at least 50 individual cells.

- **Feature Engineering:** For each dataset, we prioritized the top 2,000 highly variable genes (HVGs) to capture the most informative transcriptional variations. Crucially, all perturbed genes were manually appended to the feature set to ensure the inclusion of primary regulatory targets.
- **Transformation:** Raw counts underwent library-size normalization and log-transformation ($X = \ln(\text{CPM} + 1)$) to stabilize variance and mitigate sequencing depth artifacts.
- **Differential Expression (DE) Profiling:** To characterize the transcriptomic impact of each perturbation, we identified differentially expressed genes (DEGs) via the Wilcoxon rank-sum test. Genes with Benjamini-Hochberg adjusted p-values below 0.05 were designated as DEGs, providing a ground-truth reference for functional response evaluation.

The Norman dataset (Norman et al., 2019) serves as a pivotal benchmark for modeling high-dimensional transcriptional responses to combinatorial genetic perturbations. This study employed CRISPR activation (CRISPRa) to systematically upregulate target genes within the human K562 leukemia cell line. The resulting Perturb-seq atlas comprises transcriptomic profiles of approximately 91,000 single cells, encompassing 105 single-gene and 131 dual-gene activations. Due to its coverage of complex genetic interactions—including synergistic, epistatic, and redundant effects—this dataset poses a significant challenge for generative models aiming to generalize from individual components to unseen combinatorial states.

To rigorously evaluate model generalization, we designed two distinct experimental settings, summarized in Fig. 7. The first, the additive setting, is designed to assess compositional generalization, where a model is trained on single-gene perturbations and must predict the effects of unseen dual-gene combinations. The second, the more challenging holdout setting, evaluates zero-shot generalization. In this scenario, a subset of genes is entirely held out from training, and the model must predict the perturbation outcomes for these unseen genes, both individually and in novel combinations. Together, these settings provide a comprehensive benchmark of a model’s ability to extrapolate beyond its training data.

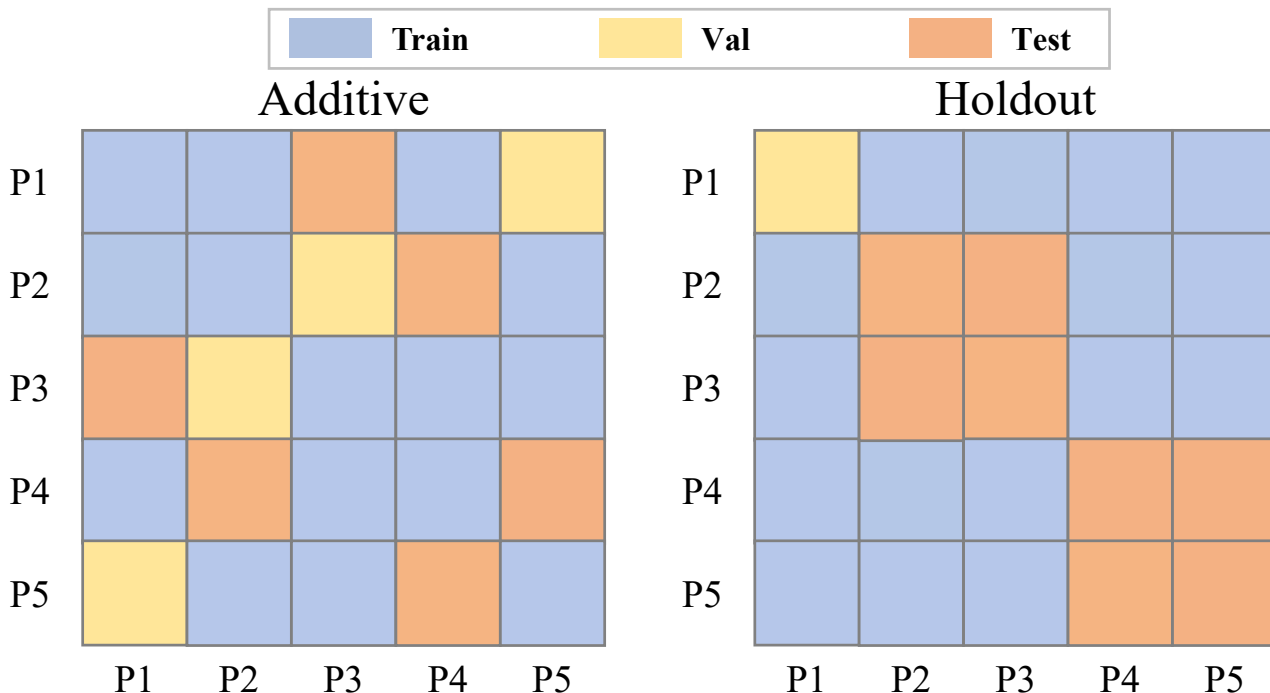


Figure 7. Overview of Experimental Settings. **Additive setting:** Evaluates the model’s ability to predict unseen dual-perturbation combinations based on observed single perturbations. **Holdout setting:** Assesses performance on both unseen single perturbations and entirely novel dual-perturbation combinations.

The Replogle2022_rpe1 dataset (Replogle et al., 2022) is an essential-gene Perturb-seq screen in the hTERT-immortalized retinal pigment epithelial (RPE1) cell line, generated by Replogle et al. (2022). Using CRISPR interference (CRISPRi), the study systematically silences common essential genes (on the order of $\sim 2.4k$ targets) and profiles transcriptomic responses at

single-cell resolution, comprising on the order of hundreds of thousands of cells. As a large-scale, high-quality Perturb-seq benchmark, it provides a rigorous testbed for generative models to predict cellular states under diverse essential gene knockdowns and to assess scalability and generalization in complex regulatory settings.

Dataset Partitioning. We partitioned the filtered perturbations into training, validation, and testing sets, adhering to the default protocol established in GEARS (Roohani et al., 2024). The training set was utilized for model fitting, while the validation set was employed for hyperparameter tuning and model selection. Finally, the testing set was reserved for an unbiased evaluation of the final model’s performance. For a detailed breakdown of the data splits, please refer to Table 10.

Table 10. Summary Statistics of Different Datasets

Metric	Norman Additive (Norman et al., 2019)	Norman Holdout (Norman et al., 2019)	Reprogle2022_rpe1 (Reprogle et al., 2022)
Number train/val/test	89926/8311/10990	92213/7905/11327	109929/11191/41999
Condition of train/val/test	167/32/32	190/21/26	1037/115/384
Test Description	Only double	Single & Double	Only single
UMI Count	2051	2051	3754
Cell Type	K562	K562	RPE1

A.3.3. REPRODUCIBILITY STATEMENT

Our code is provided in the supplementary materials, including the complete implementation framework. To ensure transparency and reproducibility, we will release all datasets, codebases, and model checkpoints, accompanied by comprehensive documentation.

A.3.4. METRIC DEFINITIONS

To comprehensively evaluate the point-prediction accuracy and distributional fidelity of our method, we employ a diverse set of metrics established in prior single-cell perturbation modeling studies, including those utilized in the Virtual Cell Challenge (Roohani et al., 2025). The evaluation protocol for the majority of these metrics remains consistent with the standard pipeline defined in `cell-evel` library.

Point-prediction Accuracy: These metrics quantify the numerical deviation between the predicted and ground-truth gene expression profiles:

- **MSE & MAE:** Mean Squared Error and Mean Absolute Error measure the cell-level or pseudobulk-level residual magnitudes.

$$\text{MSE} = \frac{1}{NG} \sum_{i=1}^N \sum_{j=1}^G (X_{ij} - \hat{X}_{ij})^2, \quad \text{MAE} = \frac{1}{NG} \sum_{i=1}^N \sum_{j=1}^G |X_{ij} - \hat{X}_{ij}| \quad (10)$$

where N and G denote the number of cells and genes, respectively.

- **L2 Distance ($L_{2,\text{mean}}$):** Measures the Euclidean distance between the predicted and observed mean expression vectors across all perturbations $p \in \mathcal{P}$.

$$L_{2,\text{mean}} = \frac{1}{|\mathcal{P}|} \sum_{p \in \mathcal{P}} \|\hat{\mathbf{y}}_p - \mathbf{y}_p\|_2 \quad (11)$$

Biological Response Fidelity To evaluate the model’s capacity to capture complex transcriptional dynamics and regulatory directions, we utilize the following metrics.

- **Pearson Δ ($\rho\Delta$) & Pearson Δ DEG ($\rho\Delta^D$):** These metrics measure the linear correlation between predicted and observed perturbation-induced transcriptional shifts, defined as $\Delta\mathbf{y} = \mathbf{y}_p - \bar{\mathbf{y}}_{\text{ctrl}}$.

$$\rho\Delta = \frac{1}{|\mathcal{P}|} \sum_{p \in \mathcal{P}} \text{Corr}(\hat{\mathbf{y}}_p - \bar{\mathbf{y}}_{\text{ctrl}}, \mathbf{y}_p - \bar{\mathbf{y}}_{\text{ctrl}}) \quad (12)$$

Specifically, $\rho\Delta^D$ restricts this evaluation to the **top 20 highly-responsive genes** (DEGs) ranked by their absolute mean difference, providing a focused assessment of the model’s ability to recover primary regulatory signals while mitigating stochastic noise.

- **Directional Accuracy (ACC Δ & ACC Δ^D):** These metrics quantify the model's precision in predicting the direction of gene expression changes (up-regulation vs. down-regulation) relative to the control state.

$$\text{ACC}\Delta = \frac{1}{|\mathcal{P}|G} \sum_{p \in \mathcal{P}} \sum_{g=1}^G \mathbb{I}[\text{sgn}(\hat{y}_{pg} - \bar{y}_{g,\text{ctrl}}) = \text{sgn}(y_{pg} - \bar{y}_{g,\text{ctrl}})] \quad (13)$$

Analogous to the correlation metrics, ACC Δ^D focuses exclusively on the most significantly perturbed gene subset (top 20 DEGs) to verify the robustness of predicted regulatory effects.

- **DE Spearman Significance (DES):** This assesses the rank consistency of log-fold changes (LFC) specifically for genes identified as statistically significant via the Wilcoxon rank-sum test ($p < 0.05$).

$$\text{DES} = \frac{1}{|\mathcal{P}|} \sum_{p \in \mathcal{P}} \text{Spearman} \left(\log_2 \frac{\hat{y}_{p,\text{sig}}}{\bar{y}_{\text{ctrl},\text{sig}}}, \log_2 \frac{y_{p,\text{sig}}}{\bar{y}_{\text{ctrl},\text{sig}}} \right) \quad (14)$$

Distributional Discriminative Power:

- **Perturbation Discrimination Score (PDS):** To evaluate if the predicted state \hat{y}_p is uniquely identifiable, we compute the rank of the true target y_p among all possible true states $\{y_t\}_{t=1}^N$ based on L_1 distance.

$$\text{PDS} = \frac{1}{|\mathcal{P}|} \sum_{p \in \mathcal{P}} \left(1 - \frac{\text{rank}_p - 1}{N - 1} \right) \quad (15)$$

A.4. Baselines

To evaluate the effectiveness of scBIG, we benchmarked it against 13 baseline models. Unless otherwise specified, the baseline models were configured with their default parameters to ensure a fair comparison.

A.4.1. CONTROL

The *Control* baseline serves as a null hypothesis, assuming that the biological system remains in a steady state despite the applied perturbation. Formally, it predicts the post-perturbation profile \hat{x} by directly adopting the empirical mean of the unperturbed control cells \bar{x}_{ctrl} :

$$\hat{x} = \bar{x}_{\text{ctrl}} \quad (16)$$

This baseline effectively quantifies the baseline variance and provides a lower bound for measuring the magnitude of perturbation-induced transcriptional shifts.

A.4.2. LINEAR

Following the benchmark framework established in (Ahlmann-Eltze et al., 2025), the *Linear* method models the transcriptomic response as a linear combination of gene-level latent features. Let \mathbf{G} be the gene embedding matrix derived from the top K ($K = 512$) principal components of the training data $\mathbf{Y}^{\text{train}}$. The model optimizes a weight matrix \mathbf{W} to minimize the reconstruction error:

$$\mathbf{W}^* = \arg \min_{\mathbf{W}} \|\mathbf{Y}^{\text{train}} - (\mathbf{G}\mathbf{W}^T + \mathbf{b})\|_2^2 \quad (17)$$

where \mathbf{b} denotes the mean expression vector. The optimal \mathbf{W} is solved via normal equations with Tikhonov regularization ($\lambda = 0.1$) to ensure numerical stability and generalization to unseen perturbations.

A.4.3. LINEAR-SCGPT

The Linear-scGPT (Ahlmann-Eltze et al., 2025) baseline adopts an identical regression architecture to the Linear method but replaces the statistical PCA components with biologically-informed embeddings. Specifically, the matrix \mathbf{G} is populated with high-dimensional gene representations extracted from the scGPT (Cui et al., 2024) foundation model. By leveraging zero-shot embeddings that capture complex gene-gene semantic relationships, this method assesses the extent to which pre-trained biological priors can enhance linear prediction accuracy.

A.4.4. GEARS

GEARS (Roohani et al., 2024) integrates gene-gene interaction graphs with a multi-layer perceptron to predict multi-gene combinatorial perturbations. We adopted the standard GEARS architecture and its built-in gene association graphs. The model was trained using the Adam optimizer with a learning rate of 10^{-3} for 20 epochs.

A.4.5. CELLORACLE

CellOracle (Kamimoto et al., 2023) facilitates *in silico* gene perturbations by integrating Gene Regulatory Network (GRN) inference with vector field analysis. We utilized the official implementation from the CellOracle repository to construct cluster-specific networks. To accommodate the smaller cell count in our control group relative to the standard tutorial datasets, we adjusted the computational parameters by reducing the number of iterations (n_iters) from 100,000 to 1,000, thereby improving computational efficiency while maintaining the integrity of the regulatory simulations.

A.4.6. SAMSVAE

samsVAE (Wu et al., 2022) leverages a variational autoencoder architecture that decouples the latent space to isolate perturbation effects from background cellular states. We applied the default KL-divergence weights and network depths during training to ensure stability in learning low-dimensional representations.

A.4.7. GRAPHVCI

GraphVCI (Bereket & Karaletsos, 2023) utilizes variational causal inference and graph neural networks to model the impact of perturbations on gene networks. We executed its official code library while maintaining the default hidden layer dimensions and regularization parameters to evaluate its recovery performance under structural constraints.

A.4.8. scGPT

scGPT (Cui et al., 2024) is a generative foundation model built on the Transformer architecture, pre-trained on millions of single cells to capture complex gene regulatory networks. For perturbation prediction, we followed the official repository's protocol for encoding perturbation conditions. The model was fine-tuned on task-specific datasets for 20 epochs using default hyperparameters, with the best-performing checkpoint selected based on validation results.

A.4.9. scFOUNDATION

scFoundation (Hao et al., 2024) is a large-scale model pre-trained on the human cell atlas, providing high-capacity gene expression embeddings. In our experiments, we utilized its pre-trained weights to extract gene embeddings and employed the GEARS (Roohani et al., 2024) framework for downstream training. The training process followed the default pipeline, ensuring that data normalization was strictly aligned with the pre-training phase.

A.4.10. GENECOMPASS

GeneCompass (Yang et al., 2024) integrates cross-species transcriptomic data to enhance sensitivity to genetic perturbations through knowledge-augmented pre-training. We utilized its pre-trained weights from the human dataset to extract embeddings and performed training within the GEARS (Roohani et al., 2024) framework. The implementation maintained the recommended optimizer settings and batch sizes as specified in the official code.

A.4.11. CELLFM

CellFM (Zeng et al., 2025) is a large-scale foundation model pre-trained on an extensive atlas of 100 million human single-cell transcriptomes, leveraging the Transformer architecture to learn comprehensive gene representations across diverse biological contexts. In our experimental framework, we utilized the pre-trained CellFM weights as a high-capacity feature extractor to derive gene-level embeddings. These biologically-informed embeddings were subsequently integrated into the GEARS (Roohani et al., 2024) model for downstream perturbation prediction. The integrated model was trained for 20 epochs using the default optimization settings to effectively align the foundation model's prior knowledge with the specific regulatory dynamics of the target dataset.

Algorithm 1 Gene-Relation Clustering (GRC)

```

1: Input: Gene embeddings  $\mathbf{E} \in \mathbb{R}^{G \times d}$ , PPI matrix  $\mathbf{A}^{\text{PPI}}$ , clusters  $K$ , iterations  $T$ .
2: Output: Balanced hard partition  $\mathcal{C} = \{c_1, \dots, c_K\}$ .
3:
4: Initialize centroids  $\{\mu_k\}_{k=1}^K$  via  $k$ -means++ on  $\mathbf{E}$ .
5: Assign initial clusters  $\mathcal{C}$  using  $D^{\text{sem}}$ .
6:
7: for  $t = 1$  to  $T$  do
8:   {// Update Cost Matrix with PPI prior}
9:   for  $i = 1$  to  $G$ ,  $k = 1$  to  $K$  do
10:     $d_{ik}^{\text{sem}} = 1 - \text{cosine}(E_i, \mu_k)$ 
11:     $d_{ik}^{\text{PPI}} = 1 - \frac{1}{|c_k|} \sum_{j \in c_k} A_{ij}^{\text{PPI}}$ 
12:     $C_{ik} = d_{ik}^{\text{sem}} + d_{ik}^{\text{PPI}}$ 
13:   end for
14:
15:   {// Optimal Transport via Sinkhorn}
16:   Set  $a = \frac{1}{G} \mathbf{1}_G$ ,  $b = \frac{1}{K} \mathbf{1}_K$ .
17:    $\Pi^* = \text{Sinkhorn}(\mathbf{C}, a, b, \epsilon)$ 
18:
19:   {// Balanced Rounding & Update}
20:    $\mathcal{C} \leftarrow \text{CapacityConstrainedRounding}(\Pi^*)$ 
21:    $\mu_k \leftarrow \text{mean}(\{E_i \mid i \in c_k\})$  for each  $k$ .
22: end for
23:
24: Return Final partition  $\mathcal{C}$ .

```

A.4.12. STATE

STATE (Adduri et al., 2025) models cellular responses as transitions within a latent manifold. In our benchmarking, we trained the STATE model from scratch using the official implementation to ensure a fair and reproducible experimental setup. We opted against using the pre-trained weights because the publicly available transition models are specifically formulated for single-agent "drug-dosage" scenarios and do not natively support the gene perturbations or combinatorial settings evaluated in this work.

A.4.13. CELLFLOW

CellFlow (Klein et al., 2025) models perturbation responses as continuous transformations between control and perturbed states using a flow-matching objective to learn a velocity field in a low-dimensional latent space. Following the official reference implementation, we first projected the gene expression data into a 50-dimensional PCA space to serve as the latent representation. During inference, the model integrates the learned flow to predict the perturbed state, which is subsequently mapped back to the full gene space via the PCA decoder for evaluation.

A.5. Pathway Analysis of Gene Clusters

To provide a more granular view of the biological identity of each gene module, we performed an extensive pathway enrichment analysis at the sub-pathway level for both the *Norman* and *Repl* datasets. Complementing the categorical summary in the main text, Figures 8 and 9 illustrate the $-\log_{10}(p\text{-value})$ of specific Reactome sub-pathways across the 32 gene clusters identified by GRC.

In the *Norman* dataset (see Figure 8), the sub-pathway distribution reveals highly specialized functional modules. For instance, Cluster 9 (C9) exhibits extreme enrichment in core cell cycle regulators such as *E2F targets*, *G2/M Checkpoint*, and *Mitotic Spindle Checkpoint*, while Cluster 3 (C3) is distinctly focused on *Eukaryotic Translation Termination*. Notably, Cluster 15 (C15) and Cluster 10 (C10) capture diverse RNA-related processes including *mRNA Splicing* and *Polyadenylation*, respectively.

Algorithm 2 Stage I: Self-supervised Pre-training (Latent Manifold Pre-training)

```

1: Input: Expression matrix  $\mathbf{X} \in \mathbb{R}^{N \times G}$ ; gene clusters  $\mathcal{C} = \{c_k\}_{k=1}^K$  from GRC; gene embeddings  $\mathbf{E} \in \mathbb{R}^{G \times d}$ ; inducing
   points  $\mathbf{I} \in \mathbb{R}^{M \times D}$ .
2: Output: Pre-trained encoder  $E_\phi$  (GCAE) and decoder  $D_\psi$ .
3: Initialize parameters  $\phi, \psi$  (and  $\mathbf{I}$  if learnable).
4: repeat
5:   Sample a batch  $\{\mathbf{x}_i\}_{i=1}^B$  from  $\mathbf{X}$ .
6:   for  $i = 1$  to  $B$  do
7:     (1) Reorder into module-structured input.
8:      $\mathbf{x}_i^{\text{mod}} \leftarrow \text{REORDERBYCLUSTERS}(\mathbf{x}_i, \mathcal{C}) \in \mathbb{R}^{K \times L}$ ,  $L = G/K$ .
9:     (2) Dual-stream fusion (expression + semantic priors).
10:     $\mathbf{h}_k^{\text{exp}} \leftarrow \text{Proj}_{\text{exp}}(\mathbf{x}_i^{\text{mod}}) \in \mathbb{R}^D$ , for  $k = 1..K$ .
11:     $\bar{\mathbf{e}}_k \leftarrow \frac{1}{|c_k|} \sum_{g \in c_k} \mathbf{E}_g$ ,  $\mathbf{h}_k^{\text{sem}} \leftarrow \text{Proj}_{\text{sem}}(\bar{\mathbf{e}}_k) \in \mathbb{R}^D$ .
12:     $\mathbf{H}_i^{(0)} \leftarrow [\mathbf{h}_1^{\text{exp}} + \mathbf{h}_1^{\text{sem}}; \dots; \mathbf{h}_K^{\text{exp}} + \mathbf{h}_K^{\text{sem}}] + \text{PosEnc}(\mathcal{C}) \in \mathbb{R}^{K \times D}$ .
13:    (3) Perceiver bottleneck: Compress–Process–Broadcast.
14:     $\mathbf{I}' \leftarrow \text{LN}(\mathbf{I} + \text{CrossAttn}(\mathbf{I}, \mathbf{H}_i^{(0)}))$ .
15:     $\mathbf{I}'' \leftarrow \text{LN}(\mathbf{I}' + \text{SelfAttn}(\mathbf{I}'))$ .
16:     $\mathbf{H}_i^{(1)} \leftarrow \text{LN}(\mathbf{H}_i^{(0)} + \text{CrossAttn}(\mathbf{H}_i^{(0)}, \mathbf{I}''))$ .
17:    (4) Cell embedding + reconstruction.
18:     $\mathbf{z}_i \leftarrow \text{Linear}\left(\frac{1}{K} \sum_{k=1}^K \mathbf{H}_{i,k}^{(1)}\right) \in \mathbb{R}^D$ .
19:     $\hat{\mathbf{x}}_i \leftarrow D_\psi(\mathbf{z}_i) \in \mathbb{R}^G$ .
20:   end for
21:    $\mathcal{L}_{\text{recon}} \leftarrow \frac{1}{B} \sum_{i=1}^B \|\hat{\mathbf{x}}_i - \mathbf{x}_i\|_2^2$ .
22:   Update  $\phi, \psi$  (and  $\mathbf{I}$  if applicable) by Adam to minimize  $\mathcal{L}_{\text{recon}}$ .
23: until convergence

```

In the *Repl* dataset (see Figure 9), where the genomic coverage is broader, we observe even more robust enrichment signatures. Cluster 15 (C15) shows a dominant association with fundamental translation machinery, including *Peptide chain elongation* and *Eukaryotic Translation Elongation*. Meanwhile, Cluster 25 (C25) and Cluster 28 (C28) effectively decouple different regulatory nodes of the cell cycle and splicing pathways.

These fine-grained heatmaps demonstrate that GRC does not merely group genes based on simple co-expression; instead, it successfully partitions them into discrete, biologically interpretable units that correspond to specific biochemical cascades. By mapping genes to these functional modules, GRC enables the model to more effectively capture and learn the intricate interactions between distinct biological modules.

A.6. Limitations and Future Work

Zero-shot Generalization and Evaluation Scope. A key goal of this work is zero-shot prediction under unseen perturbations. We evaluate this capability on two representative Perturb-seq benchmarks, Norman and RPE1, and explicitly focus on held-out perturbations to probe generalization. While these results provide evidence of transfer beyond seen interventions, they do not fully cover the diversity of real-world perturbation regimes and experimental settings. Extending evaluation to broader multi-context resources—spanning additional cell types, protocols, and intervention classes—will be important for establishing robustness at scale.

Gene Programs and Module Induction. Our approach emphasizes program-level organization by inducing gene modules via Gene-Relation Clustering (GRC) and using them as a structured scaffold. This design improves interpretability and supports efficient module-aware attention, but the induced partition remains a simplified and largely static approximation of gene-program structure. Module granularity (e.g., the choice of K) and the dependence on external signals (pretrained gene embeddings and PPI priors) may not fully capture context-specific programs that shift across cell states or perturbation regimes. An important direction for future work is to develop context-adaptive or learnable module induction mechanisms, allowing program structure to adjust to condition-specific data.

Algorithm 3 Stage II: End-to-End Conditional Flow Matching with Structure-Aware Alignment

```

1: Input: Pre-trained encoder/decoder ( $E_\phi, D_\psi$ ); vector field  $v_\theta$ ; training pairs  $(\mathbf{x}_0, \mathbf{x}_1, p)$ ; perturbation embedding  $\mathbf{c}(p)$  (ESM2); clusters  $\mathcal{C}$ ; pathway membership matrix  $\mathbf{S} \in \{0, 1\}^{P \times G}$ ; weights  $(\lambda_{\text{corr}}, \lambda_{\text{pathway}})$ ; OT regularization  $\epsilon$ .
2: Output: Fine-tuned parameters  $\{\phi, \psi, \theta\}$  (scBIG).
3: Precompute / cache target statistics for efficiency:
4: For each perturbation condition  $p$ : compute and cache  $\mathbf{R}_{gt}^*(p)$  and  $\mathbf{y}_{gt}^*(p)$ .
5:  $\mathbf{R}_{gt}^*(p) \leftarrow \text{PEARSONCORR}(\text{CLUSTERAGG}(\mathbf{x}_1, \mathcal{C}))$  (cluster-level correlation target).
6:  $\mathbf{y}_{gt}^*(p) \leftarrow \mathbf{S} \mathbf{x}_1$  (pathway activation target; optionally averaged over cells with condition  $p$ ).
7: repeat
8:   Sample a batch  $\{(\mathbf{x}_0, \mathbf{x}_1, p)_i\}_{i=1}^B$  and sample  $t_i \sim \mathcal{U}(0, 1)$ .
9:   for  $i = 1$  to  $B$  do
10:    (1) Encode control/perturbed cells.
11:     $\mathbf{z}_0 \leftarrow E_\phi(\mathbf{x}_0), \mathbf{z}_1 \leftarrow E_\phi(\mathbf{x}_1)$ .
12:    (2) Flow matching regression on linear path.
13:     $\mathbf{z}_t \leftarrow (1 - t)\mathbf{z}_0 + t\mathbf{z}_1$ .
14:     $\mathbf{u} \leftarrow (\mathbf{z}_1 - \mathbf{z}_0), \hat{\mathbf{u}} \leftarrow v_\theta(\mathbf{z}_t, t, \mathbf{c}(p))$ .
15:     $\mathcal{L}_{\text{flow}}^{(i)} \leftarrow \|\hat{\mathbf{u}} - \mathbf{u}\|_2^2$ .
16:    (3) Decode predicted endpoint via ODE solve.
17:     $\hat{\mathbf{z}}_1 \leftarrow \text{ODESOLVE}(\mathbf{z}_0, v_\theta, \mathbf{c}(p))$  (integrate to  $t=1$ ).
18:     $\hat{\mathbf{x}}_1 \leftarrow D_\psi(\hat{\mathbf{z}}_1)$ .
19:    (4) Cluster Correlation Alignment loss  $\mathcal{L}_{\text{corr}}$ .
20:     $\bar{\mathbf{x}}_1 \leftarrow \text{CLUSTERAGG}(\hat{\mathbf{x}}_1, \mathcal{C}) \in \mathbb{R}^K$  (e.g., mean per cluster).
21:     $\mathbf{R}(\hat{\mathbf{x}}_1) \leftarrow \text{PEARSONCORR}(\hat{\mathbf{x}}_1) \in \mathbb{R}^{K \times K}$ .
22:     $\mathcal{L}_{\text{corr}}^{(i)} \leftarrow \|\mathbf{R}(\bar{\mathbf{x}}_1) - \mathbf{R}_{gt}^*(p)\|_F$ .
23:    (5) Pathway-informed OT loss  $\mathcal{L}_{\text{pathway}}$ .
24:     $\hat{\mathbf{y}} \leftarrow \mathbf{S} \hat{\mathbf{x}}_1 \in \mathbb{R}^P, \mathbf{y}^* \leftarrow \mathbf{y}_{gt}^*(p)$ .
25:     $\mathcal{L}_{\text{pathway}}^{(i)} \leftarrow \mathcal{W}_\epsilon(\hat{\mathbf{y}}, \mathbf{y}^*)$  (Sinkhorn OT distance).
26:   end for
27:    $\mathcal{L}_{\text{flow}} \leftarrow \frac{1}{B} \sum_{i=1}^B \mathcal{L}_{\text{flow}}^{(i)}, \mathcal{L}_{\text{corr}} \leftarrow \frac{1}{B} \sum_{i=1}^B \mathcal{L}_{\text{corr}}^{(i)}, \mathcal{L}_{\text{pathway}} \leftarrow \frac{1}{B} \sum_{i=1}^B \mathcal{L}_{\text{pathway}}^{(i)}$ .
28:    $\mathcal{L}_{\text{total}} \leftarrow \mathcal{L}_{\text{flow}} + \lambda_{\text{corr}} \mathcal{L}_{\text{corr}} + \lambda_{\text{pathway}} \mathcal{L}_{\text{pathway}}$ .
29:   Update  $\{\phi, \psi, \theta\}$  by Adam to minimize  $\mathcal{L}_{\text{total}}$ .
30: until convergence

```

Structural Priors and Foundation Representations. scBIG incorporates multiple sources of prior information, including pretrained gene embeddings, PPI-derived structure, curated pathway memberships, and ESM2-based perturbation embeddings. These components provide strong biological grounding, but they also make performance sensitive to the quality, coverage, and context-mismatch of the underlying resources. Static priors can be incomplete, and representation errors can propagate into module induction and the biological-consistency objectives. We view scBIG as a flexible framework where such priors are modular components; future iterations could incorporate confidence-aware weighting, context-specific graph construction, or data-driven refinement of priors to improve robustness.

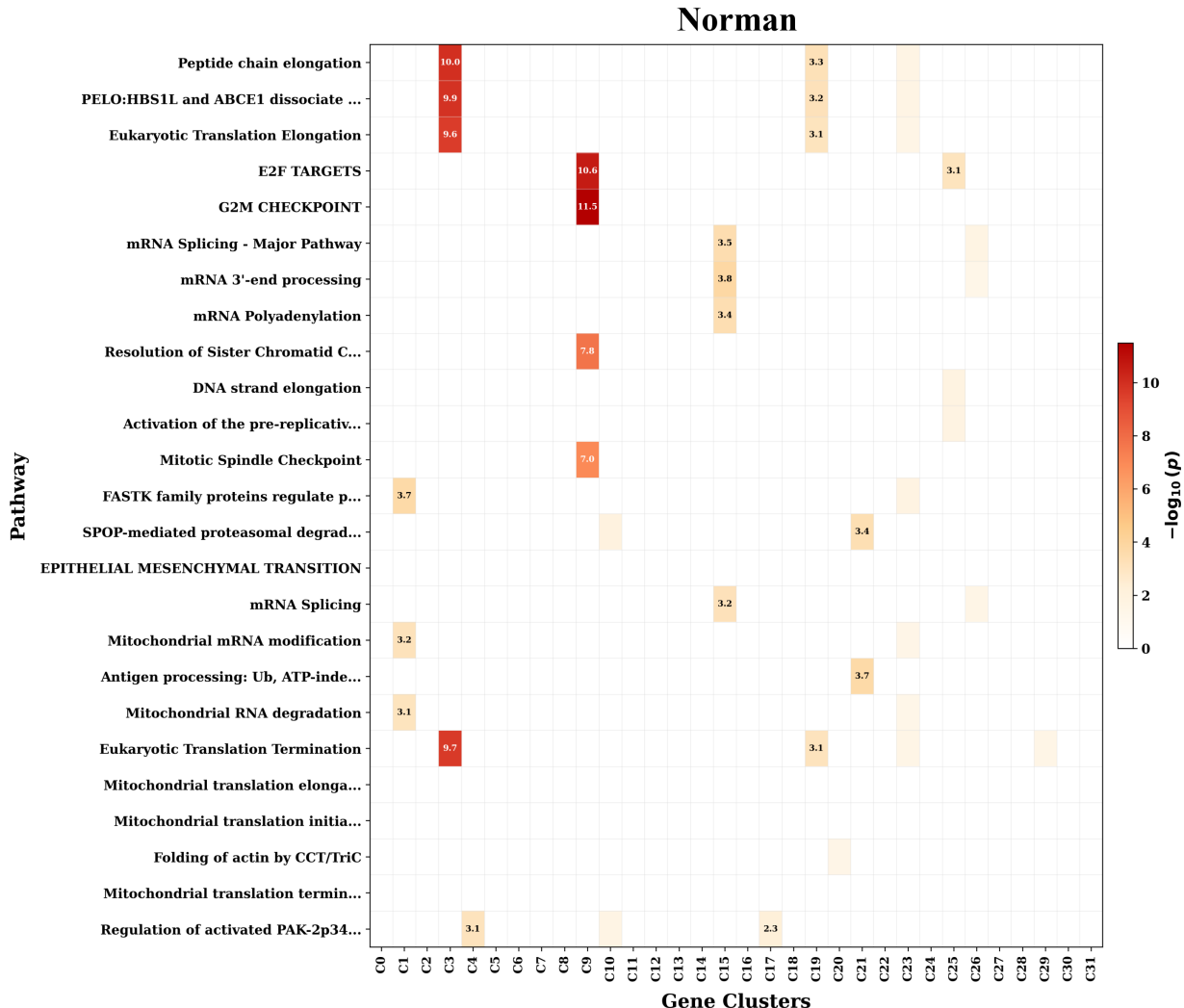


Figure 8. Pathway Enrichment of Gene Clusters on the Norman Dataset

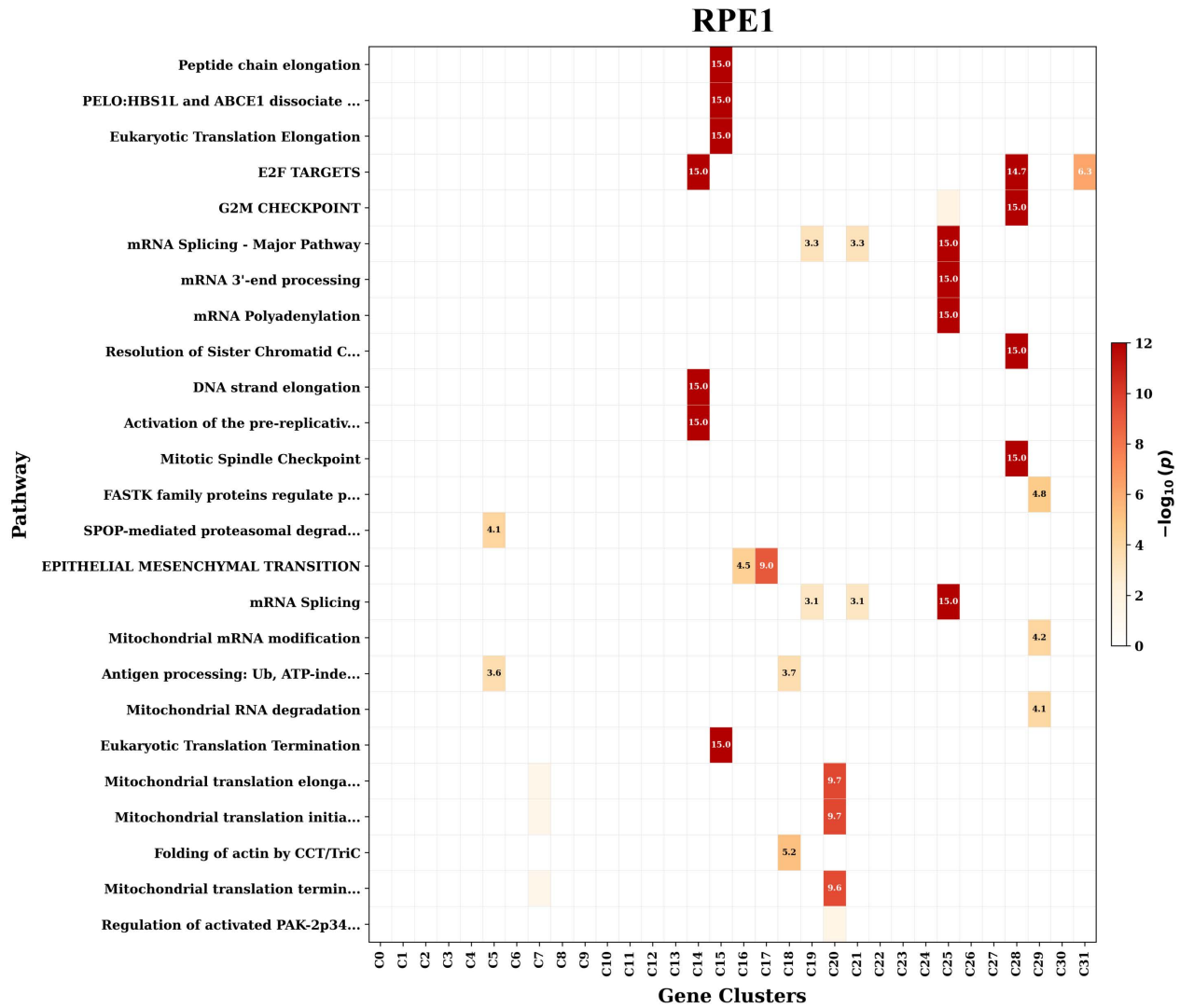


Figure 9. Pathway Enrichment of Gene Clusters on the RPE1 Dataset